ADVANCED HEALTHCARE MATERIALS
www.advhealthmat.de

# Multienzyme (3-in-1)-Mimicking a Single Nucleobase-Derived Bionanozyme for Versatile Environmental and Biomedical Applications

*Subrat Vishwakarma, Om Shanker Tiwari, Durba Banerjee, Linda J. W. Shimon, Amit Israelstam, Ilia Kaminker, Sudip Mukherjee, Ehud Gazit,* and Pandeeswar Makam**

**The quest for efficient, robust, and sustainable solutions in environmental remediation and advanced biosensing has catalyzed significant interest in biomimetic enzymology. Here, a new Bionanozyme, synthesized from a single nucleobase—adenine (A)—coordinated with copper (Cu) in a 2D crystalline structure (A-Cu), is presented. This state-of-the-art A-Cu Bionanozyme, inspired by natural redox enzymes (Laccase (LAC), Catechol oxidase (CO), and Peroxidase (POD)), is synthesized via simple and scalable, green methods including solvent-free co-grinding and natural aqueous evaporation process. A-Cu's unique structure exhibits triple-enzyme-mimicking catalytic activity, enabling it to detect and degrade toxic phenols in contaminated water and perform ultrasensitive colorimetric biosensing for key biomarkers like dopamine, hydrogen peroxide, and glutathione. Additionally, its biocompatibility and reactive oxygen species (ROS) scavenging properties highlight its potential in biomedical applications. Hence, this report provides a foundational framework for developing next-generation multienzyme-mimicking Bionanozymes with the potential to enhance eco-friendly technologies in both environmental and biomedical applications.**

## 1. Introduction

The exploration of sustainable solutions in environmental remediation and the development of sophisticated biosensing technologies have led to the burgeoning field of biomimetic enzymology.[1–6] Enzymes, exemplified by laccases (LACs)[7] catechol oxidases (CO),[8,9] and peroxidases (PODs),[10,11] play fundamental roles in diverse biological processes, exhibiting extraordinary efficiency in catalyzing redox reactions essential for cell biology (**Figure 1a**).[12–15] LACs facilitate lignin degradation, a critical step in nutrient cycling mediated by microorganisms, and promote plant growth.[16] In addition, COs further contribute to plant defense by catalyzing the oxidation of catechol's into quinones. The PODs, another ubiquitous enzyme class, encompass diverse cellular functions, including detoxifying reactive oxygen species (ROS) generated during stress responses.[17] Notably, the remarkable versatility of these enzymes fueled significant interest in their application for environmental remediation and biosensing technologies. The secret to their exceptional performance lies in their intricately tailored active sites, meticulously designed by specific amino acid residues arranged around metal cofactors to facilitate electron transfer.[18–21] Nitrogen-rich histidine residues often dominate

S. Vishwakarma, P. Makam
Department of Chemistry
Indian Institute of Technology (BHU)
Varanasi, UP 221005, India
E-mail: pandeeswar.chy@itbhu.ac.in

O. S. Tiwari, E. Gazit
The Shmunis School of Biomedicine and Cancer Research
The George S. Wise Faculty of Life Sciences
Tel Aviv University
Tel Aviv 6997801, Israel
E-mail: ehudg@post.tau.ac.il

D. Banerjee, S. Mukherjee
School of Biomedical Engineering
Indian Institute of Technology (BHU)
Varanasi, UP 221005, India

L. J. W. Shimon
Department of Chemical Research Support
Weizmann Institute of Science
Rehovot 7610001, Israel

A. Israelstam, I. Kaminker
School of Chemistry
The Sackler Faculty of Exact Sciences
Tel Aviv University
Tel Aviv 69978, Israel

E. Gazit
Department of Materials Science and Engineering
The Iby and Aladar Fleischman Faculty of Engineering
Tel Aviv University
Tel Aviv 6997801, Israel

E. Gazit
Sagol School of Neuroscience
Tel Aviv University
Tel Aviv 6997801, Israel

The ORCID identification number(s) for the author(s) of this article can be found under https://doi.org/10.1002/adhm.202501435



**DOI: 10.1002/adhm.202501435**

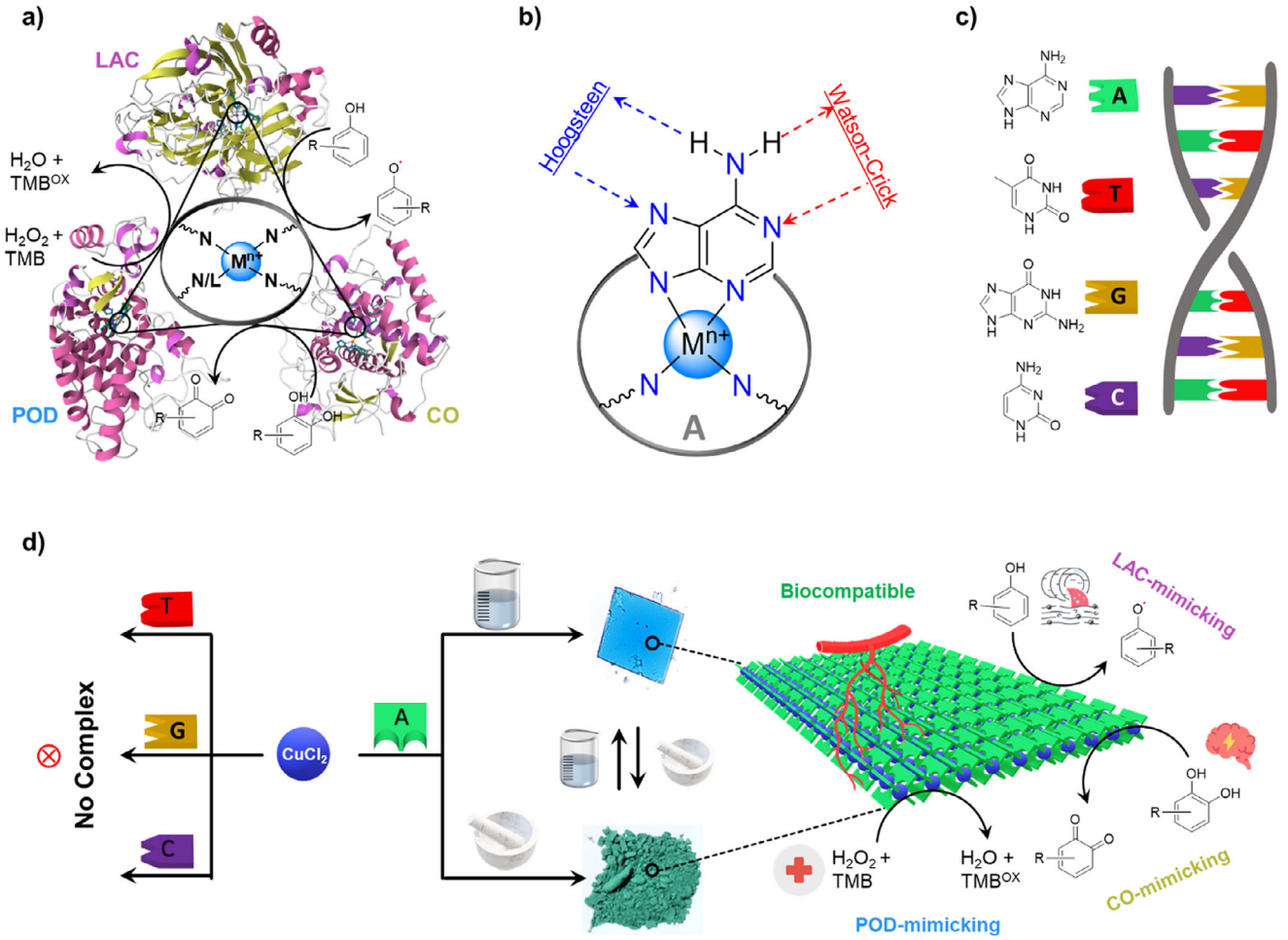


**Figure 1.** Bioinspired design strategy of minimalistic multienzyme-mimicking A-Cu Bionanozyme. a) The crystal structures of oxidoreductase enzymes such as Laccases (LACs), Catalases (COD), and Peroxidases (POD) exhibit a common primary coordination sphere at their catalytic sites, facilitating biocatalytic reactions. b) The adenine (A) structure demonstrates its ability to form hydrogen bonds (utilizing both Hoogsteen and Watson-Crick interactions), which supports supramolecular structures and metal coordination, similar to the primary coordination sphere of oxidoreductase enzymes. c) A schematic representation of the DNA double helix structure illustrates the Watson-Crick hydrogen bonding interactions between nucleobases. d) A schematic illustration shows the selective green synthesis methods (including both aqueous solvent evaporation and solvent-free mechanical co-grinding) used for creating A-Cu 2D crystalline Bionanozyme, highlighting its multienzyme mimicking biocatalytic properties and its diverse environmental and biomedical applications.

the primary coordination sphere, directly interacting with the redox-active metal ion ($Cu^{2+}$/$Fe^{3+}$).[22,23] For instance, in LACs, the copper ion's primary coordination sphere comprises four ligands: two histidine's, one cysteine, and an axial ligand.[16] Similarly, CO holds a binuclear copper center coordinated by six histidine residues.[24,25] PODs, on the other hand, utilize a heme group as the catalytic center coordinated by a histidine residue and a water molecule.[26,27] The precise arrangement of these amino acids within the active site dictates the enzyme's catalytic activity and substrate specificity.[10] However, their intricate structures and sensitivity to harsh environments pose challenges for large-scale implementation.[28] This is where biomimicry enters the stage, offering a captivating avenue to capture the catalytic prowess of enzymes within synthetic systems.[29]

The prospering field of nanomaterials has yielded a fascinating subset-nanozymes.[30,31] These materials possess enzymatic-like catalytic properties, sparking considerable interest as potential synthetic enzyme replacements. Their inherent advantages, including unparalleled stability, economic viability, and tunable catalytic activity, render them promising alternatives to natural enzymes.[32,33] However, the current landscape of nanozymes predominantly features inorganic-based materials that diverge significantly from their natural counterparts' intricate architecture and functional characteristics.[34,35] Additionally, harsh synthetic conditions, intricate fabrication processes, potential toxicity, and limited specificity pose significant challenges to integrating these nanozymes into biomedical applications.[36] To surmount these limitations, a bioinspired approach has emerged—the *de novo* design of biomolecular supramolecular nanoassemblies endowed with enzyme-like catalytic properties, termed Bionanozymes.[21,37–41] This paradigm has witnessed remarkable progress in recent years, culminating in the development of several successful Bionanozymes that faithfully mimic the active sites and catalytic functions of natural enzymes like

aldolases, LACs, PODs, and hydrolases.[42,43] By deciphering the structure–function relationships within these biomolecule-based nanoassemblies, researchers can potentially unlock the secrets of natural enzymes, paving the way for the rational design of novel, functional, and tailor-made Bionanozymes.[44–49] However, in pursuing Bionanozyme development, prior studies have predominantly focused on peptides and single enzyme mimics tailored for environmental or biosensing applications. In this study, we engineered a bioinspired minimalistic multienzyme-mimicking Bionanozyme for biomedical and environmental monitoring applications.[50,51] This innovative biomimetic strategy capitalizes on adenine, a selected component recognized for its structural adaptability and chemical attributes (Figure 1b,c).[52] Adenine (A), one of the DNA and RNA nucleobases, exhibits intrinsic biocompatibility, biodegradability, and a penchant for specific molecular recognitions through Watson-Crick and Hoogsteen hydrogen bonding, facilitating the formation of stable and robust supramolecular nanostructures.[53] Furthermore, as copper (Cu) exemplifies, adenine's functional groups, such as amines, enable facile binding and activation of metal ions.[54] Notably, adenines are recognized for their capacity to form dinuclear complexes through N3 and N9 bridging modes,[55] resulting in a coordination complex that emulates the active sites of numerous enzymes, wherein metal ions play pivotal roles in catalysis. This innovative Bionanozyme offers a synergistic combination of simplicity, sustainability, robustness, and scalability.

Guided by the pursuit of simple and sustainable practices, the Adenine-coordinated copper Bionanozyme (A-Cu) synthesis was accomplished through green synthesis methodologies, namely solvent-free mechanochemical and aqueous solution approaches. The A-Cu Bionanozyme was systematically characterized through a comprehensive analysis employing spectroscopic and microscopic techniques. The catalytic assays, simulating the activities of multiple enzymes (LAC, CO, and POD), were rigorously assessed utilizing established chromogenic substrates. Moreover, the A-Cu Bionanozyme demonstrated robust multienzyme-like catalytic activity, showcasing its efficacy in remedying environmentally hazardous phenolic compounds. More importantly, its application as an ultrasensitive biosensor for the detection of neurotransmitters such as dopamine (DA), hydrogen peroxide ($H_2O_2$), Glutathione (GSH), biocompatibility, and in vivo ROS scavenging was successfully demonstrated (Figure 1d).

## 2. Results and Discussion

### 2.1. Synthesis and Characterization of Single Nucleobase-Derived Bionanozyme

This study investigates the interaction between $CuCl_2$ and various nucleobases, specifically adenine (A), cytosine (C), thymine (T), and guanine (G), with the aim of synthesizing a nucleobase-based Bionanozyme. Due to its insolubility in water, G was excluded from the study. Notably, the mixture of A with an aqueous solution of $CuCl_2$ resulted in a distinct color change, yielding a vivid greenish-blue hue, which was not observed with cytosine or thymine under identical experimental conditions. To elucidate the nature of the interaction between $Cu^{2+}$ ions and the nucleobases, we employed ultraviolet–visible (UV–vis) absorption spectroscopy (**Figure 2a**). $CuCl_2$ exhibited a broad absorbance band in the visible region, featuring a maximum wavelength ($\lambda_{max}$) at 820 nm, characteristic of a d–d transition. In contrast, the individual nucleobase solutions—A, C, and T—displayed no absorbance bands within the visible range (600–1000 nm). Significantly, the introduction of C or T did not alter the absorption characteristics of $CuCl_2$, which maintained its $\lambda_{max}$ at 820 nm. Remarkably, the reaction mixture involving A and $CuCl_2$ demonstrated a significant blue shift ($\Delta\lambda_{max}$ = 120 nm), transitioning from $\lambda_{max}$ = 820 nm to $\lambda_{max}$ = 691 nm. This shift indicates the formation of an A-Cu complex, suggesting an induced $t_2geg$ transition. A Job plot analysis, which mapped the absorbance at 691 nm against the mole fraction of A, revealed an intersection point at 0.6 (Figure 2b). This finding indicates the formation of a stable complex between A and $Cu^{2+}$ at a 2:1 stoichiometric ratio (A: Cu). Moreover, the slow evaporation of the A and $CuCl_2$ mixture led to the formation of intense, blue-colored crystals. In contrast, no crystalline structures were observed for C or T under comparable conditions. These results underscore the selective complexation of A with $Cu^{2+}$ ions in aqueous solution, facilitating crystal formation, a phenomenon not seen with the other nucleobases studied. High-resolution scanning electron microscopy (HR-SEM) of the drop-casted reaction mixture, which used a 2:1 molar ratio of adenine precursor (A) to $Cu^{2+}$, revealed the formation of uniform, thin two-dimensional nanosheets with lateral dimensions of ≈100 µm (Figure 2c and Figure S1a–h, Movie S1, Supporting Information). This morphology indicates well-controlled crystal growth. Energy-dispersive X-ray (EDX) analysis (Figure 2d and Figure S2a–c, Supporting Information) confirmed the presence of copper (Cu), carbon (C), nitrogen (N), and oxygen (O) within the nanosheets. Elemental mapping (Figures S2d–g, Supporting Information) showed a consistent distribution of all elements across the nanosheet surface. Notably, no aggregation of Cu was observed, suggesting successful integration into the structure. The composite map (Figure S2h, Supporting Information) further demonstrated the co-localization of C, N, O, and Cu. These findings validate the successful synthesis of compositionally homogeneous A-Cu two-dimensional sheets. The uniform dispersion of Cu, a key redox-active center, is particularly crucial for enhancing catalytic efficiency, highlighting its potential applications in catalysis. Additionally, optical microscopy corroborated the formation of uniformly shaped, square 2D-plate microcrystals of the adenine-Cu complex following the slow evaporation of the solvent (Figure 2e and Figure S1i–l, Supporting Information). Consequently, single-crystal X-ray diffraction (SCXRD) analysis was employed to elucidate the precise atomic arrangement of A-Cu. The data confirmed an orthorhombic crystal system with a Cmca space group for A-Cu crystals (Figure S3, Table S1, Supporting Information). The structure determination revealed the presence of the complex cation $[Cu_2(A)_4Cl_2]^{2+}$ within the unit cell (Figure 2f–h). This complex ion exhibits 2/m crystallographic symmetry, featuring Cu atom dimers (Cu–Cu distance 3.055 Å) bridged by four A-type ligands. Each ligand coordinates with the Cu atoms through nitrogen atoms N (3) and N (9), similar to the primary coordination sphere structure of LACs, COD, and PODs. Notably, the individual $Cu^{2+}$ centers adopt a distorted square-pyramidal geometry coordinated by four nitrogens two N (9) and two N (3)) and a chloride ion occupying the apical position. An intricate hydrogen-bonding network is

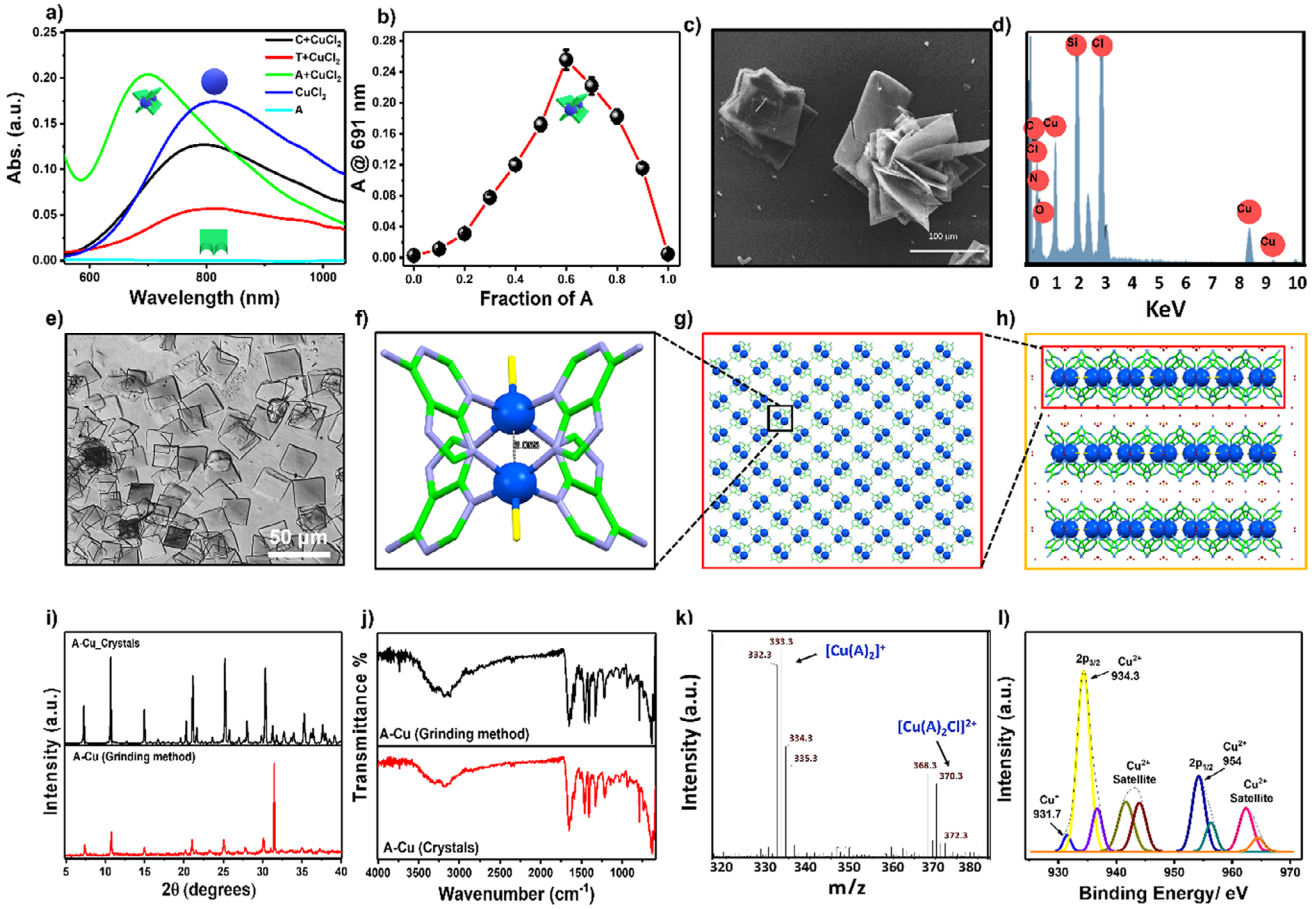


**Figure 2.** Structural characterizations of A-Cu Bionanozyme. a) UV–visible absorption spectra of $CuCl_2$, nucleobases, and their mixtures in water. b) Job plot showing the relationship between the fraction of A and absorbance at 691 nm. c) High-resolution scanning electron microscopy (HR-SEM) images of A-Cu. d) Energy-dispersive X-ray (EDX) spectra recorded from the surface of A-Cu 2D structures. e) Optical microscopy images of A-Cu 2D crystals. f–h) Single-crystal X-ray diffraction (SCXRD) structural analysis of A-Cu crystals: the primary A-Cu coordination complex structure showing Cu–Cu distance of 3.055 Å (f) and the infinite 2D layered A-Cu complex organization along the crystallographic *b*-axis (g) and *c*-axis (h). i) Comparison of powder X-ray diffraction (PXRD) patterns of A-Cu synthesized by two methods: crystals grown from solvent evaporation and those formed by solvent-free grinding. j) Comparison of Fourier-transform infrared (FT-IR) A-Cu spectra synthesized via solvent evaporation and solvent-free grinding. k) High-resolution mass spectrometry (HR-MS) spectra of A-Cu synthesized using the solvent-free grinding method. l) Selected area X-ray photoelectron spectroscopy (XPS) spectra of A-Cu.

established between chloride ions and water molecules. This network involves linkages of the type O-H—N, N-H—O, and O-H—Cl, interacting with all non-coordinated nitrogen atoms of the A ligands. Furthermore, these layers are tightly packed through hydrogen-bonded interactions with interleaved water molecules, ultimately forming a highly stable, multilayered structure in the bulk A-Cu Bionanozyme.

In addition, a solvent-free mechanical co-grinding (solid powders of A and $CuCl_2$) technique was employed to synthesize the A-Cu complex. The powder X-ray diffraction (PXRD) pattern of the mechanically synthesized material was then compared to a simulated PXRD pattern generated from single-crystal X-ray diffraction (SCXRD) data of A-Cu (Figure 2i and Figure S4, Supporting Information). The PXRD patterns exhibited a high degree of similarity, indicating successful synthesis of the complex through mechanical co-grinding. Furthermore, Fourier transform infrared (FT-IR) spectroscopy revealed a close match between the peak positions of the mechanically ground A-Cu sample and single crystals grown from an aqueous solution (Figure 2j). These combined findings provide unambiguous evidence that solvent-free mechanical grinding effectively yields the A-Cu complex with similar molecular packing and interactions consistent with crystals grown from an aqueous solution. Furthermore, high-resolution mass spectrometry (HR-MS) analysis of A-Cu synthesized by solvent-free mechanical co-grinding method shows characteristic peaks at *m*/*z*-333.3 and *m*/*z*-370.3 corresponds to $[Cu(A)_2]^+$ and $[Cu(A)_2Cl]^{2+}$ unit in A-Cu molecule that directly correlates with the SCXRD structural data of A-Cu (Figure 2k and Figure S5, Supporting Information). Next, X-ray photoelectron spectroscopy (XPS) analysis was performed to investigate the oxidation state of copper and identify the binding energies of all constituent elements within the A-Cu 2D sheets. The XPS analysis (Figure 2l and Figure S6, Supporting Information) confirmed the presence of C, N, O, Cu, and Cl with atomic ratios of 46.92%, 37.37%, 3.79%, 5.19%, and 6.73%, respectively. The high binding energy peaks observed at 934.3 eV ($Cu2p_{3/2}$)

and 954.1 eV ($Cu2p_{1/2}$) in the Cu2p spectrum are characteristic of $Cu^{2+}$.[56–61] These peaks are accompanied by the corresponding $Cu^{2+}$ satellite peaks at 962.5 and 941.5 eV, further supporting the presence of $Cu^{2+}$ in the A-Cu 2D sheets. Notably, peak 931.7 confirms the presence of $Cu^{+}$ in A-Cu and $Cu^{2+}$. This reveals that A-Cu is a mixed-valence Bionanozyme containing both $Cu^{2+}$ and $Cu^{+}$-like natural enzyme laccase active site.

### 2.2. LAC-Mimicking Assay of A-Cu Bionanozyme for Detecting and Removing Toxic Phenolic Pollutants from Water

Following the synthesis of enzyme-inspired A-Cu 2D assemblies, we investigated their LAC-mimicking biocatalytic properties by employing the well-established chromogenic reaction involving 2,4-dichlorophenol (DP) and 4-aminoantipyrine (AP) (**Figure 3a**). Upon introduction of A-Cu into a mixture of colourless AP and DP solution (PBS buffer, pH of 7.4), the reaction mixture underwent a visible transformation into an intense red solution (Figure S7a, Supporting Information).[22] Analysis of the UV–visible absorption spectra of the resultant red solution revealed a distinctive broad UV–visible absorbance band cantered at $\lambda max$ = 512 nm, attributed to the formation of oxidized red dye anti-pyrilquinoneimine as the product (Figure 3b).[62] Control experiments conducted under analogous conditions (A, $Cu^{2+}$, DP+AP, A+$Cu^{2+}$, A+DP+AP) failed to exhibit significant product formation, A-Cu Bionanozymes displayed 100% activity compared to the $Cu^{2+}$ which shows only 30% activity (Figure 3c). These findings indicate the exclusive LAC mimicking catalytic role of A-Cu in the oxidation of DP, subsequently reacting with AP to generate the anti-pyrilquinoneimine dye product. To visually monitor the progression of A-Cu Bionanozyme catalysed oxidation of DP, in situ, microscopy experiments were conducted at 15-s intervals over 1 h (Movie-S2 and Figure S9, Supporting Information). Observation revealed the transformation of the initial colourless reaction mixture into a vibrant red color on the surface of the 2D A-Cu crystals while maintaining their morphology. This provides additional visual confirmation of the catalytic functionality of the A-Cu 2D crystals. Furthermore, filtration experiments (Figure S7b, Supporting Information) did not demonstrate significant formation of the red dye product or its characteristic absorbance band, thereby indicating that the catalytic function is solely attributable to A-Cu 2D sheets and excludes any potential release of $Cu^{2+}$ ions during catalysis or contributions from dissolved or non-assembled structures. The catalytic oxidation of DP by A-Cu Bionanozyme was monitored by varying the substrate concentration (0.02–0.6 mM) while maintaining fixed optimum concentrations of 4-aminophenol (AP) and A-Cu (Figure S7c–e, Supporting Information). A-Cu Bionanozyme effectively catalyzed the reaction, as evidenced by increased absorbance at 512 nm. The corresponding kinetic profiling of initial reaction velocity ($V_0$) versus DP concentration followed the Michaelis–Menten (MM) equation, a well-established model in enzyme kinetics. The sigmoidal trend of $V_n$ with increasing DP concentration (Figure 3d) suggests cooperative binding. Kinetic parameters obtained from the MM fitting revealed an MM constant ($K_m$) of 0.04431 mM, a maximum catalytic reaction velocity ($V_{max}$) of 6.17 × 10–5 mM $s^{-1}$, and a calculated catalytic rate constant ($k_{cat}$) value of 1.199 $s^{-1}$.[27] Notably, the combination of a lower $K_m$ and a higher $V_{max}$ than that of natural LAC enzyme underscores the superior LAC-mimicking ability of the A-Cu Bionanozyme (Table S2, Supporting Information). Interestingly, the solvent-free mechanical co-grounded A-Cu Bionanozyme also exhibited comparable catalytic activity as that of A-Cu single crystals, highlighting the viability of this synthetic approach (Figure S7f, Supporting Information). The superior LAC-mimicking ability of A-Cu Bionanozyme paves the way for its application as a visual colorimetric probe for DP detection in water. The linear relationship between DP concentration (20–200 μM) and absorbance at 512 nm resulted in an impressive limit of detection (LOD) of 7.8 μM (Figure 3e and Figure S7g, Table S3, Supporting Information). Additionally, A-Cu demonstrated effective catalytic oxidation of various environmentally harmful phenols (Figure 3f), producing noticeable red products. Fascinatingly, 2,4,6-trichlorophenol, one of the most hazardous pollutants, exhibited the most intense red coloration. Furthermore, the LAC-like catalytic performance of A-Cu Bionanozyme was evaluated in various real water samples, including tap water, river water, and seawater (Figure S7h, Supporting Information). Notably, A-Cu exhibited consistent catalytic efficiency for DP oxidation across all tested water matrices, highlighting its potential for environmental monitoring and water treatment applications. For practical deployment, long-term storage stability is a critical factor. To assess its durability, the A-Cu Bionanozyme was stored under standard conditions and monitored over an extended period (Figure S7i, Supporting Information). Remarkably, it retained 99% of its relative catalytic activity even after 30 days, demonstrating exceptional stability. These findings underscore the suitability of A-Cu Bionanozyme for real-world applications, particularly in sustainable environmental remediation. Additionally, the recyclability of the A-Cu Bionanozyme was evaluated through a laccase-like catalytic assay by using phenol DP along with reagent AP. After each cycle, the Bionanozyme was recovered by centrifugation at 12000 rpm for 10 min, followed by thorough rinsing with double-distilled water before being reused. Remarkably, the A-Cu Bionanozyme retained more than 95% of its relative catalytic activity up to nine consecutive reuse cycles (Figure S8a, Supporting Information). These findings underscore the suitability of A-Cu Bionanozyme for real-world applications, particularly in sustainable environmental remediation.

The catalytic center of laccases consists of four copper sites, classified into three distinct types: T1, T2, and binuclear copper cluster comprising T3.[63] The enzymatic mechanism of laccase involves substrate oxidation, electron transfer, and the reduction of molecular oxygen ($O_2$) to water ($H_2O$), all occurring at these copper-active sites. During the catalytic cycle, the redox interplay between monovalent ($Cu^{+}$) and divalent ($Cu^{2+}$) copper facilitates electron shuttling from reducing substrates to oxygen. To explore the laccase-mimicking catalytic mechanism of A-Cu Bionanozyme, we conducted a series of experiments. Electron paramagnetic resonance (EPR) spectroscopy was employed to analyze the redox states of copper within A-Cu during catalysis (Figure 3g). As confirmed by X-ray photoelectron spectroscopy (XPS) data, A-Cu exhibited a strong EPR signal at 3300 G, further indicating the presence of the $Cu^{2+}$ state in A-Cu. Interestingly, this signal intensity notably decreased upon adding the DP substrate to the reaction mixture. This interaction leads to the oxidation of the phenolic substrate to quinones, accompanied by

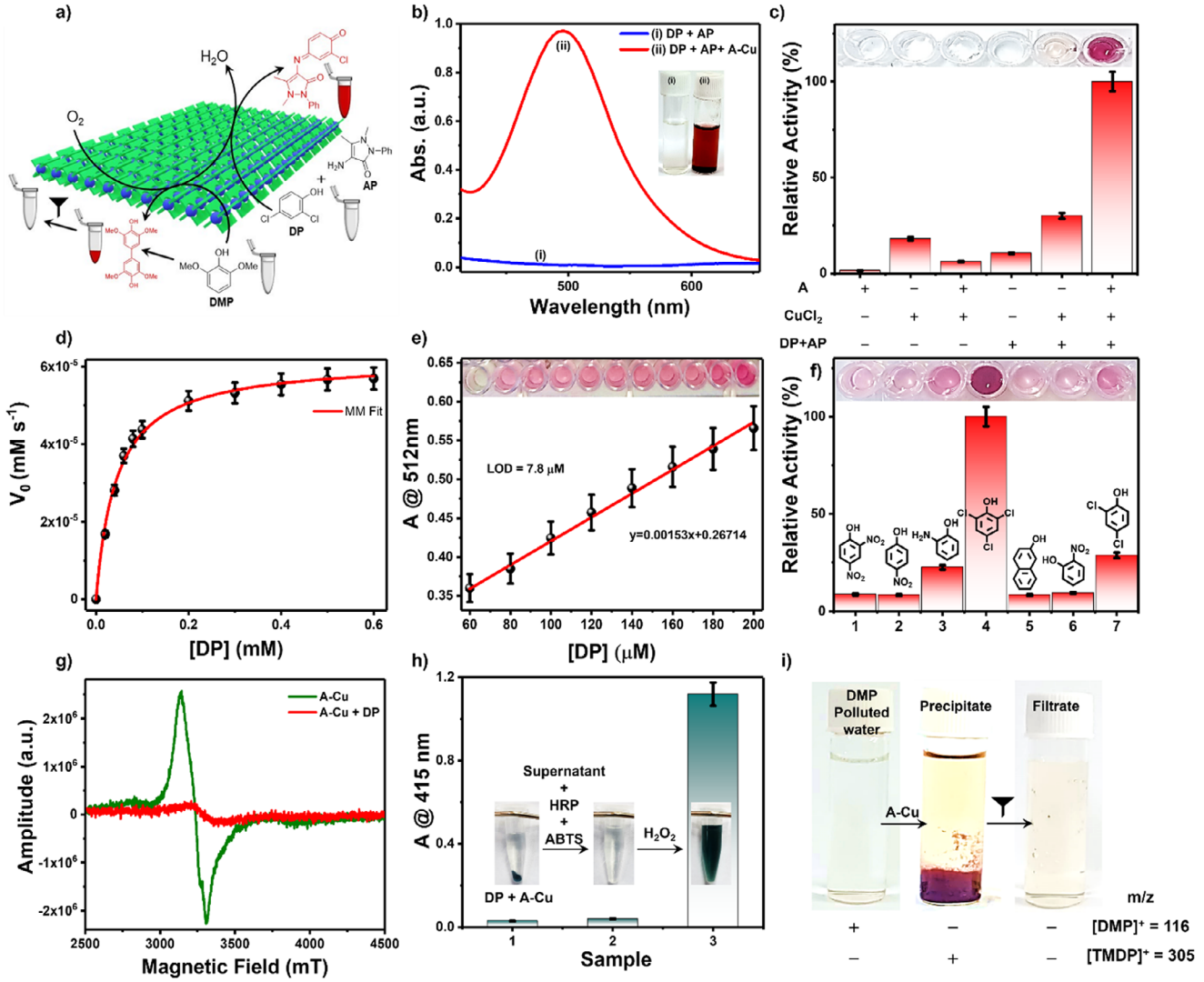


**Figure 3.** LAC-mimicking catalytic assay of A-Cu Bionanozymes and their applications in environmental remediation. a) The schematic illustration of the LAC-mimicking catalytic characteristics of the A-Cu Bionanozyme used for the detection and removal of phenol from water. b) The UV–vis absorption spectra of the substrates (DP+AP) are presented both in the presence and absence of A-Cu (in PBS buffer at pH 7.4). The inset includes corresponding photographs of the reaction vials. c) Relative catalytic activity is shown in control experiments, with data from three independent tests ($n = 3$). Inset: corresponding photographs of the reaction wells. d) The initial reaction rate ($V_0$) catalyzed by A-Cu (0.1 mg mL$^{-1}$) as a function of substrate concentration, with [DP] ranging from 0 to 0.6 mM and [AP] at 0.5 mM ($n = 3$ independent experiments), fitted using the Michaelis–Menten model. e) A standard linear curve correlates absorbance at 512 nm with the concentration of DP. Inset: corresponding photographs of the reaction wells. f) The comparison of relative catalytic conversion activity of the A-Cu Bionanozyme is shown for various toxic phenolic pollutants, listed from left to right: 1) 2,4-Dinitrophenol, 2) 4-Nitrophenol, 3) 2-Aminophenol, 4) 2,4,6-Trichlorophenol, 5) 2-Naphthol, 6) 2-Nitrophenol, and 7) 2,4-Dichlorophenol. Inset: corresponding photographs of the reaction wells. g) Selected area electron paramagnetic resonance (EPR) spectra of the A-Cu Bionanozyme depicted before and after the addition of DP. h) Control experiments examine the in situ production of $H_2O_2$ as a byproduct, utilizing the HRP and ABTS enzymatic assay. Inset: corresponding photographs of the reaction vials. i) Photographs of DMP-polluted water samples, after the addition of the A-Cu Bionanozyme and the filtrate water samples and their corresponding $m/z$ mass signals. Error bars in all graphs represent the standard deviations from three independent measurements.

the reduction of $Cu^{2+}$ to $Cu^{+}$, forming the $Cu^{+}$ active site. To assess the role of molecular oxygen in the catalytic mechanism of A-Cu Bionanozyme, we performed the reaction in both oxygen-rich and oxygen-depleted environments (the latter achieved by bubbling nitrogen gas through the reaction mixture). Remarkably, A-Cu exhibited a tenfold higher catalytic oxidation rate of DP in the presence of oxygen compared to the oxygen-depleted conditions, clearly demonstrating oxygen's involvement in the catalytic process (Figure S8b, Supporting Information). Unlike other copper-containing oxidases, such as glucose oxidase, which generate hydrogen peroxide ($H_2O_2$) as a byproduct during phenol oxidation, laccases directly reduce $O_2$ to water.[64] To confirm the nature of the oxygen reduction product, we incubated a reaction mixture containing DP (excluding 4-AP to prevent red interference) with A-Cu for 20 min, followed by centrifugation (Figure 3h). The resulting supernatant was treated with

ABTS and horseradish peroxidase (HRP), a standard colorimetric system for $H_2O_2$ detection.[65] Interestingly, no significant color change or absorbance shift was observed (Figure 3h inset), indicating the absence of $H_2O_2$ as a byproduct. However, upon the addition of exogenous $H_2O_2$ as a positive control, the solution immediately turned green, displaying a distinct absorbance peak at 415 nm, corresponding to the oxidized ABTS product. Based on these findings, we propose a laccase-like catalytic mechanism for A-Cu Bionanozyme, illustrated in Figure S10 (Supporting Information).[66] The catalytic cycle comprises four key steps: 1) substrate binding, 2) substrate oxidation, 3) $O_2$ binding, and 4) $O_2$ reduction. Initially, phenolic substrates bind to the binuclear $Cu^{2+}$ site within A-Cu. This is followed by substrate oxidation to a semiquinone radical, which undergoes further electron rearrangement to form a quinone, accompanied by the reduction of $Cu^{2+}$ to $Cu^{+}$. Subsequently, molecular oxygen binds to the binuclear $Cu^{+}$ site, forming a $Cu^{+}$–$O_2$ complex. Finally, oxygen is reduced to water, and $Cu^{+}$ is reoxidized to $Cu^{2+}$, thereby completing the catalytic cycle of A-Cu Bionanozyme.

In order to expand the potential applications of the A-Cu Bionanozyme, we investigated its catalytic capacity for the removal of the phenolic compound 2,6-dimethoxyphenol (DMP) from aqueous solutions (Figure S11, Supporting Information). Notably, the introduction of A-Cu to the colorless DMP-contaminated water resulted in the formation of a water-insoluble red precipitate (Figure 3i). Following centrifugation, the reaction mixture was filtered and analyzed both the red precipitate and the resulting filtrate using electrospray ionization mass spectrometry (ESI-MS). The initial DMP-contaminated water sample revealed a prominent monomeric DMP ion peak at $m/z = 116$. In contrast, the red precipitate predominantly exhibited a peak at $m/z$ 305, which corresponds to the dimeric product TMDP, catalyzed by A-Cu (Figure 3i and Figure S12–S15, Supporting Information). Importantly, the filtrate did not contain any detectable traces of $m/z$ peaks of either DMP or TMDP, indicating the successful removal of DMP contamination from the water through LAC-mimicking catalytic oxidation facilitated by A-Cu. These findings underscore the potential of A-Cu Bionanozyme for the selective visual detection and removal of harmful phenolic pollutants from water.

## 3. CO-Mimicking Assay of A-Cu Bionanozyme for Colorimetric Detection of Dopamine

After successfully demonstrating LAC-mimicking catalytic activity of the A-Cu Bionanozyme, we further investigated its potential for catalyzing the oxidation of catechol's via mimicking the catechol oxidase (CO) like activity.[25] Catechol oxidation to o-quinone is essential in various fields, including environmental protection and medical diagnostics. It is mainly used to detect neurotransmitters such as dopamine (DA), and abnormal concentration of DA which is associated with various neurological disorders.[67] To evaluate the CO-mimicking catalytic activity of A-Cu, we selected well-established 3,5-di-tert-butylcatechol (3,5-DTBC) as a model substrate (**Figure 4a**).[8,9] Upon introducing A-Cu into a colorless aqueous solution of 3,5-DTBC (PBS buffer, pH 7.4), the reaction mixture visibly transformed into an intense yellow solution (Movie S3, Supporting Information), attributed to oxidized product formation (Figure 4b). Control experiments lacking key components (A, $Cu^{2+}$, 3,5-DTBC combinations) showed no significant product formation, confirming the exclusive role of A-Cu in catalyzing 3,5-DTBC oxidation to 3,5-DTBQ (Figure 4c). The pH-dependent studies showed the optimum activity at pH-7 and 8 (Figure 4d). Subsequently, a catalytic assay was conducted by varying the 3,5-DTBC concentration (0.02–1.0 mM) while maintaining a constant and optimum concentration of A-Cu (Figure 4e and Figure S16, Supporting Information).

The initial reaction rate ($V_0$) followed the MM equation, revealing a $K_m$ of 0.592 mM, $V_{max}$ of 0.0848 mM $min^{-1}$ and calculated $k_{cat}$ value of 78.8 $min^{-1}$ (Figure 4e). These kinetic parameters suggest superior CO-mimicking catalytic activity compared to previously reported studies (Table S4, Supporting Information). The CO-like catalytic mechanism of the A-Cu Bionanozyme bears similarities to the LAC-like mechanism, as illustrated in Figure S17 (Supporting Information).[66,68,69] This process encompasses four essential steps in the catalytic cycle: 1) substrate binding, 2) substrate oxidation, 3) molecular oxygen binding, and 4) oxygen reduction. Initially, catechol substrates attach to the binuclear $Cu^{2+}$ site within the A-Cu structure. Following this, the substrate undergoes oxidation to form a quinone, with the simultaneous reduction of $Cu^{2+}$ to $Cu^{+}$. Next, molecular oxygen binds to the now reduced $Cu^{+}$ site, resulting in the formation of a $Cu^{+}$–$O_2$ complex. Finally, this complex undergoes reduction, converting the bound oxygen into water while reoxidizing $Cu^{+}$ back to $Cu^{2+}$. This sequence of reactions completes the catalytic cycle of the A-Cu Bionanozyme. The remarkable CO-mimicking capability of A-Cu opens opportunities for its use as a visual colorimetric DA probe in water. The linear correlation between DA concentration and absorbance at 475 nm resulted in an impressive limit of detection (LOD) of 4.8 µM in the lowest concentration range (Figure 4f and Figure S18, Table S5, Supporting Information). In addition, in situ microscopy experiments monitored the oxidation process at 15-s intervals for 1 h (Figure 4g and Movie S3, Supporting Information). The colorless reaction mixture initially turned yellow, specifically on the 2D A-Cu crystal surface, visually confirming the catalytic oxidation.

## 4. POD-Mimicking Assay of A-Cu Bionanozyme for the Detection of $H_2O_2$ and GSH

The POD-mimicking biocatalytic activity of the A-Cu Bionanozyme was evaluated using hydrogen peroxide ($H_2O_2$) and the benchmark POD substrate 3,3′,5,5′-tetramethylbenzidine (TMB). As shown in **Figure 5a**, the catalytic decomposition of $H_2O_2$ by the A-Cu Bionanozyme converts to $H_2O$; during this reaction, colorless TMB molecules are oxidized to a deep blue chromogenic product ($^{ox}$TMB), which shows a characteristic absorbance at 652 nm (Movie S4, Figure S20a, Supporting Information).[70] Upon the addition of A-Cu to a colorless mixture of $H_2O_2$ and TMB in PBS buffer (1X, pH 4, at 24 °C), an immediate color change to deep blue was observed, along with a broad absorbance band in the visible region with $\lambda_{max}$ at 652 nm (Figure 5b). This confirms the intrinsic POD-mimicking biocatalytic capability of the A-Cu Bionanozyme. In contrast, control solutions containing $H_2O_2$, TMB, A-Cu alone, and combinations of $H_2O_2$+TMB, $H_2O_2$+A-Cu, and TMB+A-Cu did not show any significant visible color change or absorbance band, indicating the absence of background reactions (Figure 5c). The pH-dependent

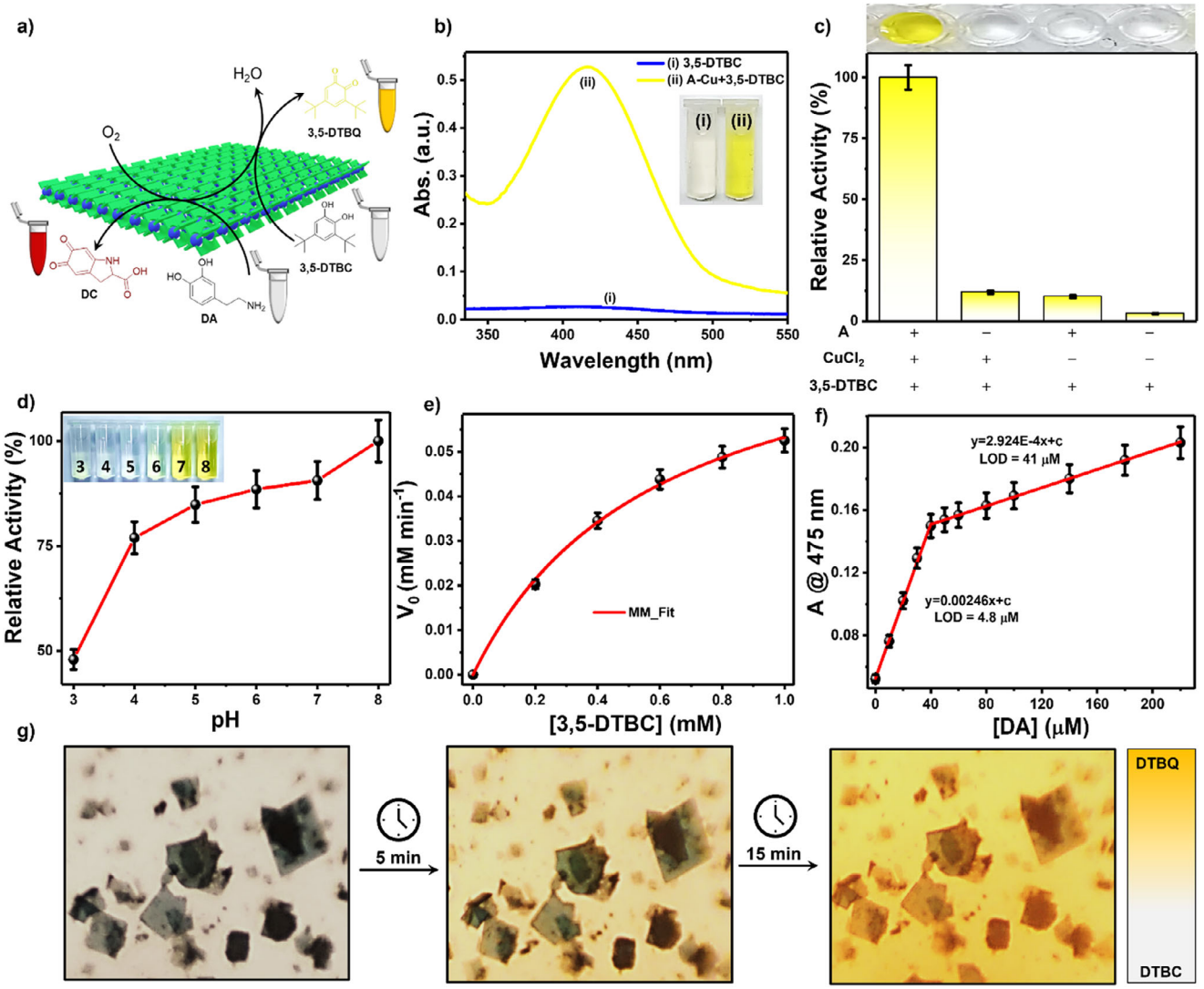


**Figure 4.** CO-mimicking catalytic assay of A-Cu Bionanozymes for ultrasensitive dopamine detection. a) Schematic illustration of CO-mimicking catalytic activity of the A-Cu Bionanozyme in detecting dopamine (DA). b) UV–visible absorption spectra of 3,5-DTBC and in the presence of the A-Cu Bionanozyme are shown, accompanied by corresponding photographs of the reaction vials in the inset. c) Relative catalytic activity is demonstrated through control experiments, with data collected from three independent trials ($n = 3$). Inset: corresponding photographs of the reaction wells. d) pH-dependent relative catalytic activity of the A-Cu Bionanozyme. Inset: corresponding photographs of the reaction vials. e) The initial reaction rate ($V_0$) catalyzed by A-Cu at a concentration of 0.1 mg mL$^{-1}$ is plotted against substrate (3,5-DTBC) concentration, and the data are fitted using the Michaelis–Menten model. f) A standard linear curve showing absorbance at 475 nm versus DA concentration. g) Optical microscopy snapshots captured at various intervals displaying the in situ monitoring of 3,5-DTBC oxidation catalyzed by A-Cu crystals (Movie S3, Supporting Information), highlighting the color change of the solution from colorless at 0 min to pale yellow after 15 min.

studies revealed that the acidic pH 4 is optimal for A-Cu POD-mimicking activity (Figure 5d). Next, the POD-activity of A-Cu was tested in acetate buffer also, it is interesting to note that more reaction progress was observed in the case of PBS buffer at optimum pH (Figure S19, Supporting Information). To elucidate the reaction kinetics, reaction rates were measured under optimum constant catalyst concentration (0.2 mg mL$^{-1}$, Figure S20b, Supporting Information) and constant optimum concentration of TMB (0.2 mM, Figure S20c, Supporting Information) with varying concentrations of substrate $H_2O_2$. The enzyme-like kinetics of the A-Cu Bionanozyme are evident from the relationship between the initial reaction rate and substrate $H_2O_2$ concentration (Figure S20d, Supporting Information). An exponential increase in reaction rate was observed, which subsequently plateaued, indicating that further increases in substrate ($H_2O_2$) concentration did not significantly impact the reaction rate. The initial reaction velocity concerning substrate concentration fits well with the MM equation (Figure 5e). From the MM fitting analysis, the maximum reaction rate ($V_{max}$) and the MM constant ($K_m$) were extracted and compared with literature values (Table S6, Supporting Information). For the substrate $H_2O_2$, A-Cu exhibited kinetic parameters with a $V_{max}$ of $8.14 \times 10^{-5}$ mM s$^{-1}$, $K_m$ of 0.0848 mM, and a calculated $k_{cat}$ value of 9.276 s$^{-1}$.[26] Notably, the lower $K_m$ and higher $V_{max}$ values for A-Cu Bionanozymes indicate a

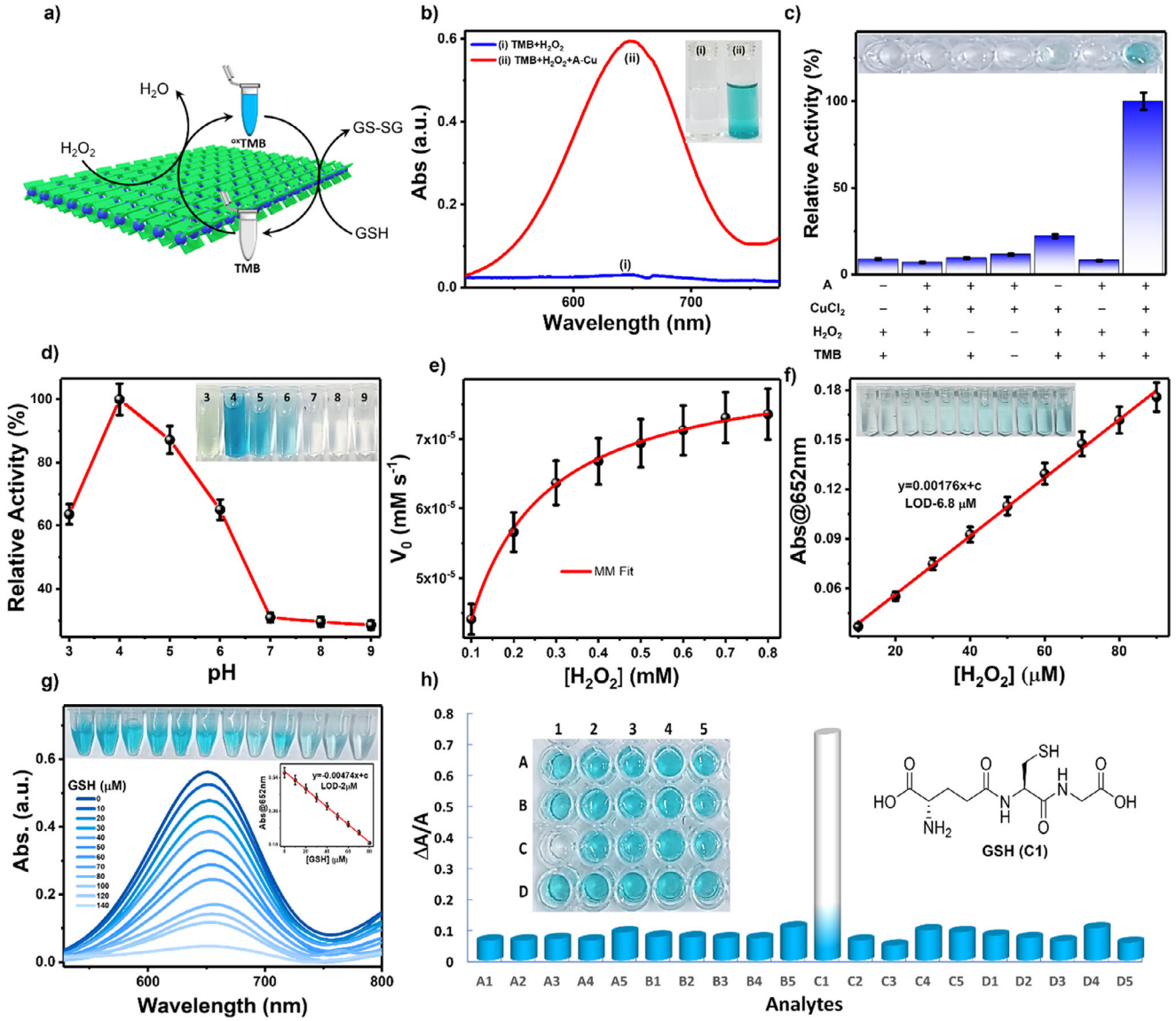


**Figure 5.** POD-mimicking catalytic assay of A-Cu Bionanozymes for $H_2O_2$ and GSH Detection. a) Schematic illustration of the POD-mimicking catalytic characteristics of the A-Cu Bionanozyme for colorimetric detection of $H_2O_2$ and GSH. b) UV–vis absorption spectra of the substrates ($H_2O_2$ + TMB) alone and in the presence of the A-Cu Bionanozyme. Inset: corresponding photographs of the reaction vials. c) The relative catalytic activity is demonstrated through various control experiments. Inset: corresponding photographs of the reaction wells. d) pH-dependent relative POD-mimicking catalytic activity of the A-Cu Bionanozyme. Inset: corresponding photographs of the reaction vials. e) The initial reaction rate ($V_0$) catalyzed by the A-Cu Bionanozyme (0.2 mg $mL^{-1}$) is plotted against the concentration of $H_2O_2$ ([TMB] = 0.2 mM), and the data are fitted using the Michaelis–Menten model. f) A standard linear curve showing absorbance at 652 nm in relation to $H_2O_2$ concentration, with corresponding photographs in the inset. g) UV–vis absorption spectra of the incremental addition of GSH to the A-Cu + $H_2O_2$ + TMB reaction mixture. The inset presents a standard linear curve showing absorbance at 652 nm against GSH concentration, along with corresponding photographs of the reaction vials. h) Interference experiment: ⊗A/A (($A_0$ – A)/A) vs various analytes. From left to right: A1 = L-Arginine, A2 = L-Lysine, A3 = L-Aspartic Acid, A4 = L-Threonine, A5 = L-Tryptophan, B1 = L-Valine, B2 = L-Alanine, B3 = L-Isoleucine, B4 = L-Serine, B5 = L-Methionine, C1 = L-Glutathione (GSH), C2 = L-Histidine, C3 = L-Phenylalanine, C4 = L-Tyrosine, C5 = L-Proline, D1 = L-Asparagine, D2 = L-Glutamine, D3 = L-Glutamic acid, D4 = L-Cysteine, D5 = L-Cystine. Inset: corresponding photograph of the reaction well plate.

higher substrate binding affinity and almost equal rate of catalysis as compared to natural HRP enzymes. To gain insight into the catalytic mechanism through which A-Cu decomposes $H_2O_2$, the involvement of reactive oxygen species (ROS) was investigated (Figure S21, Supporting Information). Superoxide radicals ($O_2^{\bullet-}$) were selectively scavenged using p-benzoquinone (PBQ), while hydroxyl radicals (OH•) were scavenged with isopropanol (IPA).[71–73] Experiments involving the co-incubation of A-Cu, $H_2O_2$, and TMB with either PBQ, IPA, or both combinations revealed a significant decrease in relative activity. Notably, IPA led to approximately a 50% reduction in activity, whereas PBQ resulted in about a 10% decrease. This suggests that both OH•

and $O_2^{\bullet-}$ play a crucial role in the oxidation of TMB. Additionally, EPR spectroscopy confirmed the presence of $OH^{\bullet}$ radicals specifically in the reaction mixture of A-Cu+$H_2O_2$ +DMPO (5,5-dimethyl-1-pyrroline N-oxide).[74] This was evident from a characteristic 1:2:2:1 quartet signal, indicative of a relatively stable paramagnetic adduct (Figure S22, Supporting Information). In comparison, control reactions involving $H_2O_2$+DMPO and DMPO did not produce significant EPR signals, further reinforcing the notion that $OH^{\bullet}$ radicals are generated during the catalytic decomposition of $H_2O_2$ by the A-Cu Bionanozyme. Hence, both the UV–vis radical scavenging experiments and EPR spectroscopy strongly suggest that both $OH^{\bullet}$ and $O_2^{\bullet-}$ contribute to TMB oxidation, thus supporting a Fenton-like catalytic mechanism for the POD-mimicking A-Cu Bionanozyme (Figure S21b, Supporting Information).[75] Furthermore, the absorbance of $^{ox}$TMB at 652 nm is directly proportional to the concentration of $H_2O_2$, enabling the quantitative assessment of $H_2O_2$ based on the catalytic activity of the A-Cu Bionanozyme. The absorbance intensity at 652 nm increased progressively with the $H_2O_2$ concentration, ranging from 10 to 140 µM (Figure S23, Supporting Information). This change was also visually apparent, transitioning from colorless to blue, as shown in Figure 5f inset, providing an immediate visual indication. A linear relationship was observed within the concentration range of 10 to 90 µM, allowing the calculation of the limit of detection (LOD) for $H_2O_2$ to be 6.8 µM (Figure 5f). Notably, this LOD is comparable to or superior to those reported for the nanozyme-based detection of $H_2O_2$ (Table S7, Supporting Information). A visual change from colorless to blue was observed concurrently with the increase in absorbance. This qualitative observation further supports the potential of the A-Cu Bionanozyme as a colorimetric probe for $H_2O_2$ detection. The results collectively underscore the efficacy of the A-Cu Bionanozyme in catalyzing the oxidation of TMB by $H_2O_2$, providing a reliable and sensitive platform for colorimetric $H_2O_2$ quantification.

### 4.1. Detection of Antioxidant Compound Glutathione (GSH)

GSH, a ubiquitous thiol-containing molecule in human tissues, is critical in maintaining intracellular redox homeostasis through the interconversion of Glutathione (GSH) to its oxidized Glutathione disulfide (GSSG).[76] Fluctuations in GSH levels are implicated in various pathologies, including cardiovascular diseases, diabetes, cancer, and neurodegenerative disorders.[77,78] Therefore, establishing rapid and accurate methods for GSH detection is crucial. Conventional GSH detection techniques often rely on reactions with its thiol group. Inspired by the robust POD-mimicking activity of A-Cu Bionanozyme, a sensing system for GSH detection was constructed using A-Cu mediated by TMB and $H_2O_2$. The proposed sensing system leverages the POD-like activity of A-Cu to oxidize TMB to its blue oxidized form ($^{ox}$TMB) in the presence of $H_2O_2$. Subsequently, GSH reduces $^{ox}$TMB to colourless TMB, generating a signal amplification effect through color change. As depicted in Figure 5g, the detection sensitivity exhibits a concentration-dependent trend with GSH. A standard curve (Figure 5g inset) constructed from the change in absorbance at 652 nm versus GSH concentration demonstrated a linear relationship within the 0–80 µM range. Moreover, upon evaluating the A-Cu+TMB+$H_2O_2$ system, the calculated LOD was 2 µM (Table S8, Supporting Information). This A-Cu-based sensing system offers superior sensitivity to existing colorimetric approaches. To evaluate selectivity, the system was challenged with various common biomolecules potentially present in biological samples, including Arginine, Lysine, Aspartic acid, Threonine, Tryptophan, Valine, Alanine, Isoleucine, Serine, Methionine, Glutathione (GSH), Histidine, Phenylalanine, Tyrosine, Proline, Asparagine, Glutamine, Glutamic Acid, cysteine and Cystine. As shown in Figure 5h, these interferences caused negligible (ΔA/A) signal changes compared to GSH, indicating excellent selectivity of A-Cu Bionanozyme toward GSH. In addition, the inset picture in Figure 5h also correlates with a change in the value of ΔA/A with color change in the case of analyte GSH (C1). GSH exhibits selective detection over cysteine, despite both being thiol (–SH)-containing compounds, due to its more complex structural characteristics. GSH possesses additional ionizable functional groups, including two carboxylic acid groups and one thiol group, which enhance its reactivity.[79–81] These features enable GSH to interact with oxidized $^{ox}$TMB more effectively than cysteine, resulting in a selective reducing capability. Hence, this work highlights the potential of A-Cu Bionanozymes for developing sensitive and selective GSH detection systems, paving the way for improved monitoring of redox status in disease contexts.

## 5. Biocompatibility and ROS Scavenging Property of A-Cu Bionanozyme

### 5.1. A-Cu Are Non-Toxic to Embryonic Fibroblast Cell Lines Evaluated by MTT Assay in a Dose-Dependent Manner

The preliminary nanocatalytic therapeutic efficiency of A-Cu Bionanozyme was evaluated in vitro through cellular cytotoxicity assays utilizing the well-established MTT (3-(4,5-dimethylthiazol-2-yl)-2,5-diphenyl tetrazolium bromide) method. The MTT assay was employed to assess the impact of A-Cu on the proliferation of the NIH3T3 embryonic fibroblast mouse cell line's (**Figure 6a**) capacity to sustain cell growth.[82] The results indicated that A-Cu did not exhibit significant cytotoxicity across a dose range of 0.1 to 0.5 mg $mL^{-1}$. However, at a higher concentration of 1 mg $mL^{-1}$, A-Cu inhibited cell proliferation, demonstrating cytotoxic effects as illustrated in Figure 6a. These findings suggest that A-Cu is biocompatible and can be safely utilized for various biological applications at treatment doses up to 0.5 mg $mL^{-1}$.

### 5.2. Application of A-Cu for the Scavenging Reactive Oxygen Species in Live Cells

The $H_2O_2$ scavenging activity of A-Cu in test tube conditions encouraged us to extend further studies in cell lines. Reactive oxygen species (ROS) scavenging using nanomaterials has been explored extensively using various cancer (KBCHR8) and normal (HEK-293T) cell lines. ROS reduction is the ability to reduce the reactive oxygen species (ROS), which significantly causes cell death due to oxidative stress.[83] Nanomaterials with ROS-inhibiting ability are biocompatible and can be employed further for other biological applications. The most common ROS is hydrogen peroxide ($H_2O_2$) in all aerobic species. To confirm the

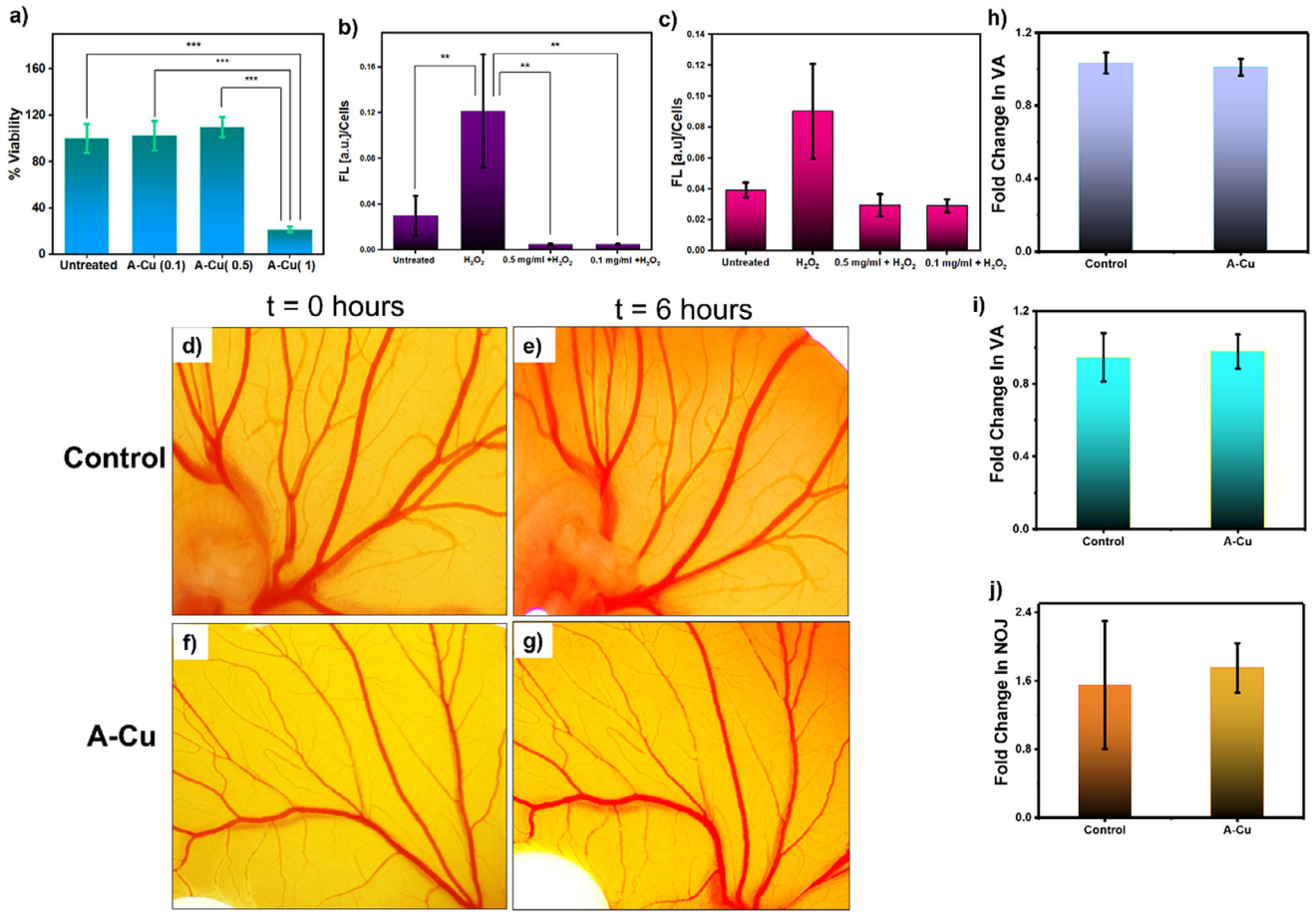


**Figure 6.** Biocompatibility and ROS scavenging studies of A-Cu Bionanozyme. a) MTT assay of A-Cu treated NIH3T3 cell lines showing cytocompatibility with varying doses. The elevated fluorescence intensity is shown by (b) KBCHR8 cells, and (c) HEK-293T with $H_2O_2$. In contrast, A-Cu at concentrations 0.1 and 0.5 mg $mL^{-1}$ showed a significant decrease in the fluorescence intensity with respect to untreated cells and cells treated with hydrogen peroxide, therefore showing efficiency in scavenging reactive oxygen species (ROS) and reducing oxidative damage. d–g) The microscopic pictures of the untreated and A-Cu treated chick embryo models at 0 and 6 h are displayed in (a–d). h–j) These figures are quantified in terms of area, length, and junction using tools such as ImageJ and Angiotool (VA denotes "Vessel Area" and NOJ denotes "Number of Junctions"). The three test results are displayed as mean ± SD. There are no appreciable differences from embryos that were not treated (*$p > 0.05$).

ROS scavenging properties of A-Cu on the removal of $H_2O_2$ in biological settings, in vitro studies were performed using cancer (KBCHR8) and normal (HEK-293T) cell lines treated with $H_2O_2$ followed by A-Cu at varying concentrations (Figure 6b,c). Each sample's fluorescence intensity was assessed following DCFDA staining, demonstrating that A-Cu displayed antioxidant activity by successfully scavenging the cellular $H_2O_2$ (Figure S24, Supporting Information). Hence, treatment of A-Cu can mitigate oxidative damage by the $H_2O_2$ scavenging activity in cell lines. The Fluorescence images representing the $H_2O_2$ scavenging activity of A-Cu are represented (**Figure 7a**).

### 5.3. A-Cu Proved to Be In Vivo Biocompatible in a Study Using Chicken Eggs

The Chorioallantoic Membrane Assay (CAM) measures alterations in blood vessel development and junctions to determine whether a material is compatible with the live tissue of fertilized chicken eggs.[84] Using a stereo microscope, blood vessel pictures of chick embryos were taken at various intervals up to 6 h after treatments were applied (Figure 6d–g). This experiment shows that A-Cu treatments did not disrupt vascular architecture or blood vessel formation in chick embryos. Numerous blood vessel integrity-related metrics, including size, length, and junctions, were quantified to show that all the parameters are constant throughout all the samples without any significant changes (Figure 6h–j). Overall, the findings are consistent with the A-Cu's biocompatibility, which is crucial for its safe biomedical applications.

### 5.4. Live Dead Assay

The cytoprotective effect of the A-Cu complex under oxidative stress was validated using a live/dead cell imaging kit, which employs Component A, calcein-AM (indicating viable cells with green fluorescence), and Component B (indicating dead cells

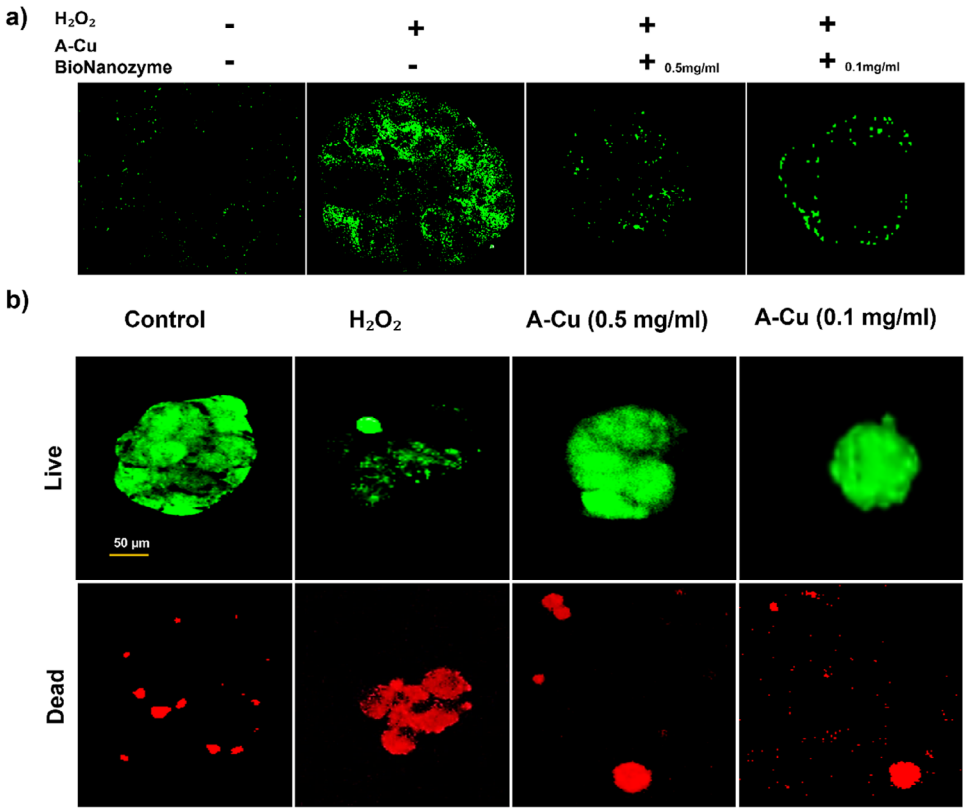


**Figure 7.** Fluorescence imaging of A-Cu scavenging reactive oxygen species in live cells and results from the Live/Dead assay. a) Treatment of HEK-293T cells with $H_2O_2$ resulted in elevated fluorescence, indicating increased levels of reactive oxygen species (ROS). Conversely, A-Cu at concentrations of 0.5 and 0.1 mg $mL^{-1}$ significantly reduced fluorescence compared to untreated cells and those treated with $H_2O_2$, demonstrating its efficacy in scavenging ROS and mitigating oxidative damage. b) The Live/Dead assay illustrated that HEK-293T cells exposed to $H_2O_2$ had a reduced number of live cells (indicated in green) and an increased number of dead cells (indicated in red). In contrast, the presence of A-Cu at concentrations of 0.1 and 0.5 mg $mL^{-1}$ in conjunction with $H_2O_2$ led to a notable increase in cell viability, further highlighting its role in reducing oxidative stress.

with red fluorescence). As shown in Figure 7b, cells treated solely with $H_2O_2$ exhibited primarily red fluorescence and minimal green fluorescence, indicating significant membrane damage and a decrease in cell viability due to oxidative injury. This finding aligns with the activation of apoptotic and necrotic pathways caused by elevated levels of reactive oxygen species (ROS).[85] In contrast, cells co-treated with A-Cu at concentrations of 0.1 and 0.5 mg $mL^{-1}$ in the presence of $H_2O_2$ demonstrated a notable increase in green fluorescence and a substantial reduction in red fluorescence. These results imply that A-Cu effectively protects cells by mitigating oxidative membrane damage and enhancing cell survival. Notably, the 0.5 mg $mL^{-1}$ dose group showed near-complete restoration of cell viability, comparable to that of untreated control cells, thereby underscoring its protective capability. Interestingly, the positive control group—which consisted of cells not exposed to either $H_2O_2$ or A-Cu—exhibited uniformly green fluorescence, suggesting a population of healthy and viable cells. The similarity in fluorescence intensity between the positive control and the A-Cu-treated groups indicates the potential of A-Cu as an effective Bionanozyme for restoring cellular homeostasis in the context of oxidative stress.

Overall, these findings highlight the dual role of the A-Cu complex as both a ROS scavenger and a cytoprotective agent. Its ability to lower ROS levels and maintain cell viability under oxidative stress positions as a promising candidate for biomedical applications aimed at addressing oxidative damage, including neurodegeneration, ischemia-reperfusion injury, and inflammatory disorders. The nanoscale integration of adenine scaffolds with copper ions likely creates a synergistic effect that combines intrinsic antioxidant properties with enzymatic mimicry.[86] Additionally, the non-toxic nature of A-Cu in control experiments suggests favorable biocompatibility, a crucial factor for its potential therapeutic applications.

## 6. Conclusions

This study presents a simple and multifunctional Bionanozyme, adenine-copper (A-Cu), synthesized through an eco-friendly, solvent-free co-grinding and aqueous evaporation method. The A-Cu Bionanozyme features a unique 2D crystalline structure and demonstrates triple-enzyme mimicking activity—laccase (LAC), catechol oxidase (CO), and peroxidase (POD)—distinguishing it from conventional single-enzyme nanozymes. Its remarkable redox versatility enables potent phenol remediation in contaminated water and highly sensitive colorimetric detection of key disease biomarkers, including dopamine, hydrogen peroxide, and glutathione. Notably, A-Cu displays superior catalytic kinetics compared to natural enzymes and retains over

95% activity after 17 catalytic cycles and 99% activity after 30 days of storage. These attributes, combined with demonstrated biocompatibility and ROS-scavenging capability, support their applicability in tissue regeneration and oxidative stress mitigation. Furthermore, its green and low-cost synthesis from adenine and copper chloride enhances scalability and economic feasibility, offering a sustainable alternative to expensive, unstable natural enzymes. Unlike previously reported nanozymes, this study uniquely integrates multi-enzyme mimicry, high biocompatibility, and robust performance into a single, scalable platform. The A-Cu Bionanozyme's combined environmental and biomedical utility marks a significant advancement in biomimetic catalysis. The implications of this work extend across water purification, biosensing, and regenerative medicine, bridging the gap between environmental and clinical applications. Future research will focus on in vivo therapeutic evaluations, deeper mechanistic studies of enzyme mimicry, and integration into smart biosensor systems for real-time diagnostics and environmental monitoring.

In summary, this research introduces a versatile, durable, and economically viable Bionanozyme with broad potential. It sets a new benchmark in green nanozyme development and paves the way for transformative advances in environmental remediation and biomedical technologies.

## 7. Experimental Section

*Materials*: Adenine, guanine, thymine, cytosine, copper chloride dihydrate, sodium hydroxide, 2,4-Dichlorophenol (DP), 4-Aminoantipyrine (AP), *N*-methyl-2-Pyrrolidone (NMP), phenol, catechol, hydroquinone, 2-aminophenol, 2-naphthol, o-nitrophenol, 2,4,6-trichlorophenol, dopamine, PBS buffer, 3,5-Ditertiary butyl catechol, hydrogen peroxide, 3,3,5,5-tetramethyl benzidine, L-glutathione, all 20 amino acids, Horseradish peroxidase enzyme (HRP) and [2,2′-azino-bis (3-ethylbenzothiazoline-6-sulfonic acid)](ABTS) were purchased from Alpha Aesar and Sigma Aldrich. Double distilled water was used to prepare all the solutions.

*Synthesis of Crystals of A-Cu Crystals*: The A-Cu Bionanozyme was synthesized by mixing solid adenine (A) (0.888 mmol) and copper chloride dihydrate ($CuCl_2{\cdot}2H_2O$) (0.444 mmol) in a molar ratio of 2:1 in 50 mL of water at room temperature. Upon the addition of (A) to copper chloride, a complex was formed, accompanied by a pronounced color change from a pale blue color to a vibrant greenish-blue shade. Subsequently, the solution underwent filtration using Whatman filter paper to eliminate any remaining contaminants that had not reacted. Afterward, the filtrate was kept in an open environment at ambient temperature in a 500 mL glass beaker to promote crystallization. Curiously, upon the evaporation of water, lustrous and vividly greenish-blue crystals formed at the base of the beaker. Crystals were collected and washed with water three to four times to remove the unreacted impurities. Finally, crystals were dried under a high vacuum and used for further studies.

*Characterization of A-Cu Bionanozyme*: **a) Optical Microscope**: The Olympus C43 microscope was used to snap pictures of A-Cu 2D crystals and to record videos of catalysis and A-Cu crystals formation as shown (Movie).

**b) UV–Visible Spectroscopy**: To study the complexation between A and $Cu^{2+}$ and all catalysis, (an Agilent Cary-60 UV–visible spectrophotometer) was used.

**c) High-Resolution Scanning Electron Microscope (HRSEM) and Energy-Dispersive X-Ray (EDX) Spectroscopy**: A-Cu samples were coated with gold after being placed on a clean microscope glass coverslip. The photographs were snapped with a JSM-6700 field emission scanning electron microscope (JEOL, Tokyo, Japan) with the voltage set to 10 kV.

**d) Fourier-Transform Infrared Spectroscopy (FT-IR)**: The synthesized A-Cu were applied onto disposable KBr infrared sample cards (Sigma-Aldrich) and then dried using a vacuum. The spectra were obtained at room temperature using a nitrogen-purged Nicolet Nexus 470 FTIR spectrometer (Nicolet) with a deuterated triglycine sulfate detector. The spectral range covered 4000 to 400 $cm^{-1}$.

**e) Single Crystal X-Ray Diffraction (SCXRD)**: Blue plate-like crystals suitable for diffraction were coated with Paratone oil (Hampton Research) mounted on MiTeGen loops and flash-frozen in liquid nitrogen. All X-ray diffraction measurements were carried out at 100 K. Diffraction measurements for A-Cu crystals were performed at the ESRF synchrotron, station ID23-1. Data were collected and processed using MXCube and the automated XDS pipeline. The structure was solved by direct methods using SHELXT-2013 or SHELXT 2016/4. The structure was refined by full-matrix least-squares against F2 with SHELXL 2016/4. The structure was illustrated using Mercury 3.9 (Cambridge Crystallographic Data Centre, Cambridge, UK).

**f) Powder X-Ray Diffraction (PXRD)**: The A-Cu nanosheets were applied onto a quartz sample holder with no background interference. Powder X-ray diffraction (XRD) analysis was conducted on a Bruker D8 Advance X-ray powder diffractometer at room temperature, with measurements taken within the 5 to 45° $2\theta$ range. The backdrop was removed to isolate the diffraction peaks.

**g) Fourier-Transform Infrared Spectroscopy (FT-IR)**: The A-Cu nanosheets were applied onto disposable KBr infrared sample cards (Sigma-Aldrich) and then dried using a vacuum. The spectra were obtained at room temperature using a nitrogen-purged Nicolet Nexus 470 FTIR spectrometer (Nicolet) with a deuterated triglycine sulfate detector. The spectral range covered 4000 to 400 $cm^{-1}$.

**h) X-Ray Photoelectron Spectroscopy (XPS)**: To confirm the elemental compositions and oxidation state of Cu metal in A-Cu, XPS spectra were collected by using XPS K-Alpha, Thermo Fisher Scientific, Central instrument facility, Indian Institute of Technology, BHU Varanasi, India. A-Cu samples were coated on a clean microscope glass coverslip and made dry to collect the XPS data.

**i) Electron Paramagnetic Resonance (EPR)**: The EPR spectra were obtained in a 5 mm flat cell at room temperature using a Bruker EMX EPR spectrometer. The recently generated A-Cu Bionanozyme, dissolved in 30 µL of water at a concentration of 1 mg $mL^{-1}$, was combined with 240 µL of PBS buffer (1X, pH 7.4). The mixture was then put into an EPR tube and rapidly froze using liquid nitrogen. The sample's pH was determined to be 7.6 using a Spintrode electrode (Hamilton). A total of 30 µL of DP solution in IPA (70 mM) was directly poured into the EPR tube. The tube was then inverted five times and frozen using liquid nitrogen. The data were plotted using the Origin software.

**j) Mass Spectrometry**: Mass spectrometry of the A-Cu complex solution was performed using an Acquity UPLC system, connected to a TQD XEVO triple quadrupole mass spectrometer with an electrospray ionization (ESI) source from Waters (Milford, MA, USA). The analysis was conducted in positive ionization mode.

*LAC-Mimicking Catalytic Assay and Kinetics Parameters Calculations of A-Cu*: **a) LAC-Mimicking Catalytic Assay of A-Cu**: To perform the LAC-mimicking catalytic assay of A-Cu, a well-known chromogenic reaction of 4-amino antipyrine (AP) with 2,4-dichlorophenol (DP) was used as a model reaction. First, AP (200 µL from 5 mM stock solution prepared in solvent IPA) and DP (200 µL 6 mM stock solution prepared in IPA) solutions were mixed with A-Cu (200 µL from 1 mg $mL^{-1}$ stock solution prepared in water) in 1400 µL PBS (1X) buffer (pH-7.4) at 25 °C. When A-Cu was added to a mixture of DP and AP a red dye product started to form. The reaction progress was monitored at 512 nm using an Agilent UV-spectrophotometer at 25 °C and continuous stirring mode.

**b) Control Studies**: Control tests were conducted by combining each component, such as AP (0.5 mM), DP (0.6 mM), Adenine (0.1 mM), $CuCl_2{\cdot}2H_2O$ (0.1 mM), and A-Cu (0.1 mM), with PBS buffer at a pH of 7.4. Curiously, no strong red hue or absorption band at 512 nm was detected in any other scenario except when (A-Cu+AP+DP) were combined.

**c) Substrate Dependent Kinetics**: Next, to perform the substrate-dependent kinetics studies, the 512 nm band was monitored with an

increase in the substrate concentration (DP). Substrate DP concentration varies (0.02, 0.04, 0.06, 0.08, 0.1, 0.2, 0.3, 0.4, 0.5, 0.6, and 0.7 mM) with fixed and optimum concentrations of AP and A-Cu in PBS buffer of pH-7.4 respectively. Furthermore, to extract the kinetic parameters like $V_{max}$ and $K_m$, the $V_0$ values were plotted as a function of substrate concentration. The $V_0$ values were plotted against substrate concentration and fitted to the Michaelis–Menten equation ($V_0 = V_{max}[S]/(K_m + [S])$) to derive the kinetic parameters $V_{max}$ and $K_m$.

**d) Substrate Scope**: The other phenolic substrates (including phenol, Catechol, Hydroquinone, 2-Aminophenol, 2,6-Dimethoxyphenol, 2-Naphthol, 2-Nitrophenol, and 2,4,6-trichlorophenol) was added in 0.6 mM of concentration (from stock solution of 6 mM prepared in IPA) were reacted with 0.5 mM AP in PBS buffer (1X, pH 7.4) that included 0.1 mg $mL^{-1}$ of A-Cu Bionanozyme with total volume of reaction mixture 2 mL.

**e) In Situ $H_2O_2$ Generation Test by Using A-Cu Bionanozyme**: A reaction mixture including DP (200 µL from stock solution of 6 mM prepared in IPA) and A-Cu (200 µL from stock solution 1 mg $mL^{-1}$ prepared in water) was added to 590 µL PBS buffer of pH-7.4. The reaction mixture was centrifuged for 10 min to distribute the catalyst A-Cu uniformly throughout the reaction mixture. Next, the enzyme horseradish peroxidase (HRP) and 2,2′-azino-bis (3-ethylbenzothiazoline-6-sulfonic acid) were added to the supernatant, but no change in color or absorbance was seen, suggesting the lack of $H_2O_2$. On the other hand, in the same set of circumstances, on adding $H_2O_2$ (10 µL from a stock solution of 50 mM prepared in water) there is a generation of a green color with strong absorbance at 415 nm, which is indicative of the oxidized ABTS product.

**f) Phenol Detection by Using A-Cu**: To conduct the DP detection experiment, varying ranges of concentration of DP (20, 40, 60, 80, 100, 120, 140, 160, 180, and 200 µM) were used with the same set of conditions as mentioned previously. After adding A-Cu to each particular sample, it was incubated for 5 min at room temperature. Next, UV–visible spectra were recorded for each sample, which shows the increasing absorbance with increasing the concentration of DP. Additionally, to calculate the limit of detection (LOD), a linear standard curve was made between absorbance at 512 nm and a concentration of DP. Interestingly, an excellent LOD = 7.8 µM was obtained in the linear range of 60 to 200 µM.

**g) pH Optimization and Storage Stability of A-Cu**: To check the pH-dependent laccase-like activity of A-Cu, identical set of conditions described in the aforementioned Section 4.1 have been employed with varying ranges of pH from 1 to 9. In addition, to check the in situ stability of A-Cu, a solution of A-Cu was prepared at a concentration of 1 mg $mL^{-1}$ to assess its storage stability. Subsequently, at intervals of 10 days, the assessments of the laccase's catalytic activity was conducted under the same conditions as previously mentioned.

**h) Separation 2,6-Dimethoxyphenol (DMP) from Water by Using the LAC-Mimicking Activity of A-Cu**: A total of 3 samples were prepared for the mass spectrometric measurements. **Sample 1** = 1 mM of DMP (400 µL, from Stock solution of 5 mM prepared in IPA) was added to 1600 µL Milli-Q water, mass spectra were recorded after well mixing of the solution. Further, A-Cu was added to the **Sample 1,** and it was incubated for 24 h. A clear red color product was obtained as a precipitate after 24 h of incubation. The red color product was filtered out and it was dissolved in the methanol. Next, the filtrate solution was labeled as **Sample 2** and precipitated dissolved in the methanol as **Sample 3**. Mass spectrometry of all the samples was recorded using an Acquity UPLC system coupled to a TQD XEVO triple quadrupole ESI source mass spectrometer system from Waters (Milford, MA, USA). Mass spectrometry was done by ESI, measuring positive ionization.

*CO-Mimicking Catalytic Assay, Kinetics, pH Studies*: **a) CO-Mimicking Assay**: To perform this experiment, 1 mM concentration of di-tert butyl catechol (3,5-DTBC) (400 µL, from 5 mM stock solution prepared in methanol) was added into 1.4 mL of PBS buffer (pH-8). When 200 µL A-Cu (from 1 mg $mL^{-1}$ stock solution which is prepared in water) was added to 3,4-DTBC, a yellow color product started to form, and the color started to saturate after 2 min. Next, the yellow-colored reaction mixture was filled in a 3.5 mL quartz cuvette to record the UV–vis spectra. It was found that the formed product shows a characteristic band at 415 nm, which shows the formation of oxidized product 3,5-di-tert-butyl-o-benzoquinone (3,5-DTBQ).

**b) Control Experiments**: Next, to perform the control experiments, the UV–visible spectra of each component were recorded individually. DTBC (1 mM), Adenine (0.1 mM), and $CuCl_2$ (0.1 mM) were added separately to PBS buffer (pH-8), and the total volume of the reaction mixture was made 2 mL. Next, UV–vis spectra were recorded for each sample, it was found that there is no absorbance band at 415 nm in all cases except DTBC+A-Cu. This experiment confirms the activity of A-Cu Bionanozyme.

**c) Substrate-Dependent Kinetics**: Next, to perform a substrate-dependent kinetics experiment, 3,5-DTBC was added (0 to 1 mM) to PBS buffer pH-8. After the addition of 0.1 mg $mL^{-1}$ A-Cu to each particular concentration of 3,5-DTBC, kinetics was recorded via monitoring the band at 415 nm. Obtained data were fitted into the Michaelis–Menten kinetics model to extract the kinetics parameters like $K_m$ and $V_{max}$ respectively.

**d) Effect of pH**: Next, the effect of pH on catechol oxidation was studied. Each sample was prepared by using 1 mM of 3,5-DTBC and A-Cu 0.1 mg $mL^{-1}$ in PBS buffer of pH (3–8) respectively and the total volume of the system was made 2 mL. UV–vis spectra were recorded for each sample; the obtained data suggested the maximum catechol oxidation at alkaline pH-8.

**e) Colorimetric Detection of Neurotransmitter Dopamine (DA) by Using CO-Mimicking Activity of A-Cu**: To perform this experiment, identical conditions were used, as described in Section 5. Next, a varying range of DA concentrations (0–200 µM) were added to PBS buffer with A-Cu (0.1 mg $mL^{-1}$). After shaking well, samples were incubated for 10 min. Next, each sample was employed for the UV–visible spectroscopy by using a 3.5 mL cuvette. Increase in absorbance at 475 nm with a rise in concentration of DA. Next, a standard curve was plotted with the concentration of DA against the Abs@475 nm. Next, LOD was calculated by using the aforementioned formula, which came to 4 µM in the lower range of DA concentration from (0–40 µM) and 41 µM in the higher concentration range of DA (40–220 µM).

*POD-Mimicking Catalytic Assay, Kinetics, and Stability Experiments*: **a) POD-Mimicking Catalytic Assay of A-Cu**: The POD activity of A-Cu was studied by using the colorimetric method. Hydrogen peroxide ($H_2O_2$) was used as a substrate and TMB was used as a colorimetric reagent. To perform this experiment, 1 mM of $H_2O_2$ (Stock solution of 50 mM in water) was added to PBS (1X) buffer of optimum pH-4, then 0.2 mM TMB (Stock solution of 21 mM in DMSO) and 0.2 mg $mL^{-1}$ of A-Cu (Stock solution of 1 mg $mL^{-1}$ in water) was added to the reaction mixture and total volume were made 2 mL. Then the sample was filled in a 3.5 mL quartz cuvette to perform the UV–visible spectra. In UV–vis spectra, an absorption band was observed at 652 nm which corresponds to $^{ox}$TMB.[87]

**b) Control Studies**: Control experiments were performed by mixing each component like $H_2O_2$ (1 mM), TMB (0.2 mM), A (0.1 mM), $CuCl_2$ (0.1 mM), and A-Cu (0.1 mM) to PBS buffer. Interestingly, there was no intense blue coloration or absorbance band observed in any other case except the combination of ($H_2O_2$ + TMB + A-Cu).

**c) pH Effect**: A combination of A-Cu (0.2 mg $mL^{-1}$), TMB (0.2 mM), and $H_2O_2$ (1 mM) was made in PBS buffers in the range of pH from 3 to 9 at room temperature. The optimum POD-like activity was at an acidic pH of 4.

**d) Substrate-Dependent Kinetics**: Next, substrate-dependent kinetics were performed by varying the concentration of $H_2O_2$ with a fixed optimum concentration of TMB, which is based on the first curve of saturated concentrations as shown in (Figure S17b, Supporting Information) (0.2 mM) and A-Cu (0.1 mg $mL^{-1}$). To determine the initial reaction rate ($V_0$), different concentrations of DP (0, 0.02, 0.04, 0.06, 0.08, 0.1, 0.2, 0.3, 0.4, 0.5, 0.6, 0.7, 0.8, 0.9, and 1 mM) were reacted with 0.5 mM of AP, catalysed by 0.1 mg $mL^{-1}$ of catalyst A-Cu. Then each sample corresponds to $H_2O_2$ and immediately records the kinetics by monitoring the band at 652 nm which corresponds to $^{ox}$TMB. The obtained data were fitted into the Michaelis–Menten model to extract the kinetics parameters $K_m$ and $V_{max}$.

**e) Detection of $H_2O_2$ by Using POD-Mimicking Catalytic Activity of A-Cu**: Concentration of $H_2O_2$ from (10, 20, 30, 40, 50, 70, 80, 90, 100, 110 µM) was added with fixed concentration of TMB (0.2 mM) and A-Cu

(0.2 mg $mL^{-1}$) in PBS buffer (pH-4) as reaction medium and total volume was made 2 mL. After the addition of the A-Cu sample was incubated for 5 min and employed for UV–vis spectra. With raises in the concentration of $H_2O_2$, there is a continuous increment of the band at 652 nm observed in UV–vis spectra. Next, to calculate the limit of detection (LOD), the standard linear curve was plotted between the concentration of $H_2O_2$ and the change in absorbance at 652 nm.

*Colorimetric Detection of Antioxidant Compound Glutathione (GSH)*: a) Variable concentrations of GSH (0, 10, 20, 30, 40, 50, 60, 70, 80, 100, 120, 140 µM) were added into the POD system which is a combination of A-Cu (0.2 mg $mL^{-1}$), TMB (0.2 mM) and $H_2O_2$ (1 mM) by maintaining same time interval of 2 min which is minimum time of saturation POD reaction progress at 25 °C. Next, after adding each concentration of GSH, UV spectra were recorded by using a 3.5 mL quartz cuvette. It was observed that on increasing GSH content the band corresponding to $^{ox}$TMB decreased continuously. Next, a plot was constructed between absorbance at 652 nm versus [GSH] (µM). A linear standard curve was obtained in the concentration range of 0–80 µM. Next, LOD = 2 µM was calculated to correspond to the minimum concentration range.

b) Interference studies were conducted by adding the concentration of 140 µM (stock solution: 1 mM solvent water) for each analyte, as determined by the maximum concentration of GSH shown in Figure 5g. These analytes were added to the peroxidase system as described in Section 4.1. Following the addition of the interfering analytes, UV–visible spectra were recorded for each sample in a PBS buffer at pH 4.0, with measurements taken at room temperature after an incubation period of 2 min for each analyte.

*Cytotoxicity and In Vivo Biocompatibility of A-Cu Bionanozyme*: **a) Using the Chorioallantoic Membrane (CAM) Experiment, Evaluate Biocompatibility of A-Cu Bionanozyme**: In this work, the CAM assay was used to inspect the biocompatibility of A-Cu on the development of blood arteries in the chicken embryo. For this experiment, fertilized eggs were obtained from a hatchery located in Varanasi, Uttar Pradesh. After that, the eggs were incubated at 37 °C for four days. The egg's outer shell was slightly punctured on the fifth day to reveal the evolving blood vessels. The chick embryo was treated with A-Cu (0.1 mg $mL^{-1}$) for 2 min at room temperature, and then Whatman filter paper discs were placed over its blood vessels. For a maximum of 6 h, the effects of A-Cu on blood vessel creation and development were seen using a Magnus MagZoom TZM6 Trinocular Stereo Zoom Microscope. Untreated eggs were used as a control. Additionally, blood artery integrity parameters like length, junctions, and size were measured using the applications Angiotool and ImageJ.[88]

**b) Investigation of Cell Viability Using the MTT Assay**: The outcome of A-Cu on the cell viability of the embryonic mouse fibroblast (NIH3T3) and Human Embryonic Kidney cell line was examined using the MTT assay. 96-well plates were seeded with 10 000/100 µL DMEM medium. Three different dosages of A-Cu (1, 0.5, and 0.1 mg $mL^{-1}$) were added as treatments after a 24-h incubation period. Following the medium removal, 100 µL (0.5 mg $mL^{-1}$) solution of MTT was included, and the combination was left to incubate for 4 h at 37 °C. The formazan crystal was dissolved by adding 100 µL of DMSO: MeOH (1:1) after discarding the MTT solutions. A multiple reader was employed to measure the absorbance of the combination at 570 nm following that, the formula below was utilized to ascertain the cell viability.

$$\% \text{ cellviability} = (\text{Absorbance}_S/\text{Absorbance}_C) \times 100 \quad (1)$$

$\text{Absorbance}_S$ and $\text{Absorbance}_C$ denote the absorbance of the sample and control at 570 nm.

**c) Measurement of Cellular Internalized ROS**: In 24-well culture dishes, cancer cells (KBCHR8.5; 20 000 cells per well) were cultivated for 24 h in the cell culture incubator, at 37 °C. Three types of cells were used to treat the cancer cell lines: untreated cells, cells with $H_2O_2$ (300 µM), and cells with varying concentrations of A-Cu. The concentrations of A-Cu used were 0.1, 0.5, and 1 mg $mL^{-1}$. After 8 h, each well received 10 µL of 2′,7′-Dichlorofluorescin Diacetate (DCFDA) (30 µM), which was then left for 30–40 min. PBS was used to properly wash the incubated cells two or three times. Following that confocal images were taken; Zeiss 510 Meta confocal microscopy equipment was used to capture images at 20×. Also, 100 µL of Radioimmunoprecipitation assay (RIPA) buffer was added to the cells to lyse them, and they were maintained for 10 min at 4 °C. Centrifuging the scraped cells for 10 min at 4 °C at 14 000 rpm yielded cell lysates. The fluorescence of both treated and untreated cells was measured using a multimode reader with an excitation at $\lambda_{ex}$ = 380 nm and an emission at $\lambda_{em}$ = 460 nm.

**d) Live Dead Assay**: Cell viability was determined using a live/dead Cell Imaging kit R37601. In accordance with the manufacturer's protocol, cells were washed with PBS twice and exposed to **Component A (Live Green)** cell-permeant calcein, AM which is hydrolyzed by intracellular esterases, and to **Component B (Dead Red)** which binds to nucleic acids. The cleavage product of calcein AM, calcein, produces a green fluorescence when exposed to 488-nm light and can be used to identify live cells. Dead red produces a red fluorescence when exposed to 570-nm light, allowing the identification of dead cells. Culture dishes were dually stained and examined under a fluorescence microscope system (Zeiss 510 Meta confocal microscopy equipment) was used to capture images of live and dead bacteria at 63 X).

**e) Statistical Analysis**: To ensure precision and credibility, the trials were carried out three times. The mean value and standard error were used to express the data from each experiment. A one-way ANOVA was performed using the Origin software to ascertain the statistical significance of the obtained data.

*Data Availability*: The X-ray crystallographic coordinates for structures reported in this study have been deposited at the Cambridge Crystallographic Data Centre (CCDC), under deposition numbers 2389408 (A-Cu). These data can be obtained free of charge from www.ccdc.cam.ac.uk/data_request/cif, the Cambridge Crystallographic Data Centre.

## Supporting Information

Supporting Information is available from the Wiley Online Library or from the author.

## Acknowledgements

P.M. acknowledges the support from ICMR, India (IIRPSG-2024-01-03827) and IIT (BHU). S.V. thanks the UGC-India and IIT (BHU) for the research fellowship. E.G. thanks to the Air Force Research Laboratories (AFRL) for support. This material is based on work supported by the Air Force Office of Scientific Research under award number FA8655-21-1-7004. Any opinions, findings, conclusions, or recommendations expressed in this material are those of the authors and do not necessarily reflect the views of the United States Air Force. S.V. and O.S.T. contributed equally to this work and are first authors.

## Conflict of Interest

The authors declare no conflict of interest.

## Data Availability Statement

The data that support the findings of this study are available in the Supporting Information of this article.

## Keywords

biomedical applications, Bionanozyme, enzyme, supramolecular assemblies

Received: April 14, 2025
Revised: June 9, 2025
Published online: June 30, 2025

[1] R. Buller, S. Lutz, R. J. Kazlauskas, R. Snajdrova, J. C. Moore, U. T. Bornscheuer, *Science* **2023**, *382*, 6673.
[2] H. Wang, Z. Zhao, Y. Liu, C. Shao, F. Bian, Y. Zhao, *Sci. Adv.* *4*, 6.
[3] L. Huang, J. Chen, L. Gan, J. Wang, S. Dong, *Sci. Adv.* **2019**, *5*, 5490.
[4] P. Makam, S. S. R. K. C. Yamijala, K. Tao, L. J. W. Shimon, D. S. Eisenberg, M. R. Sawaya, B. M. Wong, E. Gazit, *Nat. Catal.* **2019**, *2*, 977.
[5] P. Makam, S. S. R. K. C. Yamijala, V. S. Bhadram, L. J. W. Shimon, B. M. Wong, E. Gazit, *Nat. Commun.* **2022**, *13*, 1505.
[6] D. Deng, K. S. Novoselov, Q. Fu, N. Zheng, Z. Tian, X. Bao, *Nat. Nanotechnol.* **2016**, *11*, 218.
[7] R. Mehra, J. Muschiol, A. S. Meyer, K. P. Kepp, *Sci. Rep.* **2018**, *8*, 17285.
[8] M. Li, J. Chen, W. Wu, Y. Fang, S. Dong, *J. Am. Chem. Soc.* **2020**, *142*, 15569.
[9] A. Neves, L. M. Rossi, A. J. Bortoluzzi, B. Szpoganicz, C. Wiezbicki, E. Schwingel, W. Haase, S. Ostrovsky, *Inorg. Chem.* **2002**, *41*, 1788.
[10] M. Gajhede, D. J. Schuller, A. Henriksen, A. T. Smith, T. L. Poulos, *Nat. Struct. Mol. Biol.* **1997**, *4*, 1032.
[11] P. Campomanes, U. Rothlisberger, M. Alfonso-Prieto, C. Rovira, *J. Am. Chem. Soc.* **2015**, *137*, 11170.
[12] W. F. DeGrado, Z. R. Wasserman, J. D. Lear, *Science* **1989**, *243*, 622.
[13] D. Li, D. Dai, G. Xiong, S. Lan, C. Zhang, *Small* **2023**, *19*, 2205870.
[14] L. Zhang, H. Wang, X. Qu, *Adv. Mater.* **2023**, *35*, 2211147.
[15] J. Sheng, Y. Wu, H. Ding, K. Feng, Y. Shen, Y. Zhang, N. Gu, *Adv. Mater.* **2023**, *35*, 2211210.
[16] L. Arregui, M. Ayala, X. Gómez-Gil, G. Gutiérrez-Soto, C. E. Hernández-Luna, M. Herrera de los Santos, L. Levin, A. Rojo-Domínguez, D. Romero-Martínez, M. C. N. Saparrat, M. A. Trujillo-Roldan, N. A. Valdez-Cruz, *MCF* **2019**, *18*, 200.
[17] S. Ray, R. Biswas, R. Banerjee, P. Biswas, *Nanoscale Adv.* **2020**, *2*, 734.
[18] Q. Liu, A. Kuzuya, Z. G. Wang, *iScience* **2023**, *26*, 105831.
[19] K. L. Duncan, R. V. Ulijn, *Biocatalysis* **2015**, *1*, 67.
[20] Y. Lu, N. Yeung, N. Sieracki, N. M. Marshall, *Nature* **2009**, *460*, 855.
[21] F. Yu, V. M. Cangelosi, M. L. Zastrow, M. Tegoni, J. S. Plegaria, A. G. Tebo, C. S. Mocny, L. Ruckthong, H. Qayyum, V. L. Pecoraro, *Chem. Rev.* **2014**, *114*, 3495.
[22] J. H. Yum, T. Kumagai, D. Hori, H. Sugiyama, S. Park, *Nanoscale* **2023**, *15*, 10749.
[23] L. E. Maley, D. P. Mellor, *Nature* **1950**, *165*, 453.
[24] C. Eicken, C. Gerdemann, B. Krebs, C. Oxidase, *Encyclopedia of Inorganic and Bioinorganic Chemistry*, Wiley, Chichester **2004**, pp. 1319.
[25] T. Klabunde, C. Eicken, J. C. Sacchettini, B. Krebs, *Nat. Struct. Mol. Biol.* **1998**, *5*, 1084.
[26] L. Gao, J. Zhuang, L. Nie, J. Zhang, Y.u Zhang, N. Gu, T. Wang, J. Feng, D. Yang, S. Perrett, X. Yan, *Nat. Nanotechnol.* **2007**, *2*, 577.
[27] B. Jiang, D. Duan, L. Gao, M. Zhou, K. Fan, Y. Tang, J. Xi, Y. Bi, Z. Tong, G. F.u Gao, N.i Xie, A. Tang, G. Nie, M. Liang, X. Yan, *Nat. Protoc.* **2018**, *13*, 1506.
[28] T. L. Poulos, *Chem. Rev.* **2014**, *114*, 3919.
[29] S. Vishwakarma, O. S. Tiwari, R. Shukla, E. Gazit, P. Makam, *Chem. Soc. Rev.* **2025**, *54*, 465.
[30] Y. Huang, J. Ren, X. Qu, *Chem. Rev.* **2019**, *119*, 4357.
[31] H. Wei, E. Wang, *Chem. Soc. Rev.* **2013**, *42*, 6060.
[32] R. Zhang, X. Yan, K. Fan, *Acc. Mater. Res.* **2021**, *2*, 534.
[33] Q. Wang, D. Astruc, *Chem. Rev.* **2020**, *120*, 1438.
[34] W. Yang, L. Zhu, M. Yang, W. Xu, *Small* **2023**, *19*, 2211210.
[35] M. S. Wang, M. H. Hecht, *J. Am. Chem. Soc.* **2020**, *142*, 15230.
[36] J. Wu, X. Wang, Q. Wang, Z. Lou, S. Li, Y. Zhu, L. Qin, H. Wei, *Chem. Soc. Rev.* **2019**, *48*, 1004.
[37] X. Zhang, Z. An, J. An, X. Tian, *Coord. Chem. Rev.* **2024**, *502*, 215601.
[38] Y. Ouyang, Y. Biniuri, M. Fadeev, P. Zhang, R. Carmieli, M. Vázquez-González, I. Willner, *J. Am. Chem. Soc.* **2021**, *143*, 11510.
[39] C. Wang, Q. Qi, W. Li, J. Dang, M. Hao, S. Lv, X. Dong, Y. Gu, P. Wu, W. Zhang, Y. Chen, J. S. Hartig, *Nat. Commun.* **2020**, *11*, 4792.
[40] L. R. Marshall, O. Zozulia, Z. Lengyel-Zhand, I. V. Korendovych, *ACS Catal.* **2019**, *9*, 9265.
[41] H. Liang, F. Lin, Z. Zhang, B. Liu, S. Jiang, Q. Yuan, J. Liu, *ACS Appl. Mater. Interfaces* **2017**, *9*, 1352.
[42] M. Zandieh, J. Liu, *Adv. Mater.* **2024**, *36*, 2211041.
[43] Y.u Chen, Y. Yang, A. A. Orr, P. Makam, B. Redko, E. Haimov, Y. Wang, L. J. W. Shimon, S. Rencus-Lazar, M. Ju, P. Tamamis, H. Dong, E. Gazit, *Angew. Chem., Int. Ed. Engl.* **2021**, *133*, 17301.
[44] C. Zeng, N. Lu, Y. Wen, G. Liu, R. Zhang, J. Zhang, F. Wang, X. Liu, Q. Li, Z. Tang, M. Zhang, *ACS Appl. Mater. Interfaces* **2019**, *11*, 1790.
[45] R. Yu, R. Wang, Z. Wang, Q. Zhu, Z. Dai, *Analyst* **2021**, *146*, 1127.
[46] J. Liu, Y. Lu, *Angew. Chem., Int. Ed. Engl.* **2005**, *45*, 90.
[47] Y. Fu, J. Zhang, X. Chen, T. Huang, X. Duan, W. Li, J. Wang, *J. Phys. Chem. C.* **2011**, *115*, 10370.
[48] Y. Fu, X. Wang, J. Zhang, W. Li, *Curr. Opin. Biotechnol.* **2014**, *28*, 33.
[49] L. Su, S. Qin, Z. Xie, L. Wang, K. Khan, A. K. Tareen, D. Li, H. Zhang, *Coord. Chem. Rev.* **2022**, *473*, 214784.
[50] Y. Kang, C. Li, H. Shi, A. Zhang, C. Huang, C. Zhou, N. Jia, **2023**, *Chin. J. Chem.* *41*, 3189.
[51] G. Wei, S. Liu, Y. K. Peng, H. Wei, *Chin. J. Chem.* **2024**, *42*, 1515.
[52] S. Verma, A. K. Mishra, J. Kumar, *Acc. Chem. Res.* **2010**, *43*, 79.
[53] F. Pu, J. Ren, X. Qu, *Chem. Soc. Rev.* **2018**, *47*, 1285.
[54] R. K. Prajapati, S. Verma, *Inorg. Chem.* **2011**, *50*, 3180.
[55] B. J. M. Leite Ferreira, P. Brandão, A. M. Dos Santos, Z. Gai, C. Cruz, M. S. Reis, T. M. Santos, V. Félix, *J. Coord. Chem.* **2015**, *68*, 2770.
[56] X. Xu, J. Wang, R. Huang, W. Qi, R. Su, Z. He, *Catal. Sci. Technol.* **2021**, *11*, 3402.
[57] M. Guan, M. Wang, W. Qi, R. Su, Z. He, *Front. Chem. Sci. Eng.* **2021**, *15*, 310.
[58] H. Rupp, U. Weser, *Biochim. Biophys. Acta, Protein Struct.* **1976**, *446*, 151.
[59] Q. Tang, Y. Li, W. Liu, B. Li, Y. Jin, *J. Mater. Sci.* **2022**, *57*, 10072.
[60] B. Ma, S. Wang, F. Liu, S. Zhang, J. Duan, Z. Li, Y. Kong, Y. Sang, H. Liu, W. Bu, L. Li, *J. Am. Chem. Soc.* **2019**, *141*, 849.
[61] J. D. Schneider, B. A. Smith, G. A. Williams, D. R. Powell, F. Perez, G. T. Rowe, L. Yang, *Inorg. Chem.* **2020**, *59*, 5433.
[62] H. Liang, F. Lin, Z. Zhang, B. Liu, S. Jiang, Q. Yuan, J. Liu, *Appl. Mater. Interfaces* **2017**, *9*, 1352.
[63] S. M. Jones, E. I. Solomon, *CMLS* **2015**, *72*, 869.
[64] G. Janusz, A. Pawlik, U. Świderska-Burek, J. Polak, J. Sulej, A. Jarosz-Wilkołazka, A. Paszczyński, *Int. J. Mol. Sci.* **2020**, *21*, 966.
[65] H. Cai, X. Liu, J. Zou, J. Xiao, B. Yuan, F. Li, Q. Cheng, *Chemosphere* **2018**, *193*, 833.
[66] H. Zhang, Y. Chen, Y. Wei, X. Zhang, H. Ma, *ACS Appl. Mater. Interfaces* **2025**, *17*, 15886.
[67] B. Kgedal, D. S. Goldstein, *J. Chromatogr. B: Biomed. Sci. Appl.* **1988**, *429*, 177.
[68] M. Güell, P. E. M. Siegbahn, *J. Biol. Inorg. Chem.* **2007**, *12*, 1251.
[69] R. Silavi, A. Divsalar, A. A. Saboury, *J. Biomol. Struct. Dyn.* **2012**, *30*, 752.
[70] T. Tsuneda, *Sci. Rep.* **2020**, *10*, 18144.
[71] W. Cao, P. Ju, Z. Wang, Y. Zhang, X. Zhai, F. Jiang, C. Sun, *Spectrochim. Acta, Part A* **2020**, *239*, 118499.
[72] S.-J. Yin, G.-Y. Chen, C.-Y. Zhang, J.-L. Wang, F.-Q. Yang, *Mikrochim. Acta* **2023**, *190*, 25.
[73] W. Song, P. Sun, J. Zhou, X. Han, Q. Dai, F. Chai, *New J. Chem.* **2023**, *47*, 15721.
[74] C. Chen, Y. Wang, D. Zhang, *Mikrochim. Acta* **2019**, *186*, 784.
[75] S. K. Padamati, T. A. Vedelaar, F. Perona Martínez, A. C. Nusantara, R. Schirhagl, *Nanomaterials* **2022**, *12*, 2422.
[76] P. Li, S. M. Lee, H. Y. Kim, S. Kim, S. Park, K. S. Park, H. G. Park, *Sci. Rep.* **2021**, *11*, 3937.

[77] J. Liu, L. Meng, Z. Fei, P. J. Dyson, X. Jing, X. Liu, *Biosens. Bioelectron.* **2017**, *90*, 69.
[78] X. Zhu, H. Li, D. Zhang, W. Chen, M. Fu, S. Nie, Y. Gao, Q. Liu, *ACS Sustainable Chem. Eng.* **2019**, *7*, 18105.
[79] L. Li, Q. Wang, Z. Chen, *Mikrochim. Acta* **2019**, *186*, 257.
[80] X. Liu, Q. Wang, Y. Zhang, L. Zhang, Y. Su, Y. Lv, *New J. Chem.* **2013**, *37*, 2174.
[81] I. Ortiz-Gómez, A. Rivadeneyra, J. F. Salmerón, I. de Orbe-Payá, D. P. Morales, L. F. Capitán-Vallvey, A. Salinas-Castillo, *BSN* **2023**, *13*, 267.
[82] D. Banerjee, S. Vishwakarma, M. Nayak, A. Upadhyay, L. Pradhan, P. Makam, S. Mukherjee, *ACS Appl. Nano Mater.* **2025**, *8*, 4263.
[83] S. R. Chowdhury, S. Mukherjee, S. Das, C. R. Patra, P. K. Iyer, *Chem. Sci.* **2017**, *8*, 7566.
[84] I. Moreno-Jiménez, G. Hulsart-Billstrom, S. A. Lanham, A. A. Janeczek, N. Kontouli, J. M. Kanczler, N. D. Evans, R. O. C. Oreffo, *Sci. Rep.* **2016**, *6*, 32168.
[85] J. Gambini, K. Stromsnes, *J. Biomed.* **2022**, *10*, 753.
[86] T. Sun, S. Xiao, M. Wang, Q. Xie, L. Zhang, C. Zhou, M. Gong, D. Zhang, *Int. J. Nanomed.* **2023**, *18*, 7901.
[87] S. Huang, G. Chen, N. Ye, X. Kou, R. Zhang, J. Shen, G. Ouyang, *ACS Appl. Mater. Interfaces* **2020**, *12*, 57343.
[88] L. Pradhan, P. Sah, M. Nayak, A. Upadhyay, P. Pragya, S. Tripathi, G. Singh, B. Mounika, P. Paik, S. Mukherjee, *J. Biol. Inorg. Chem.* **2024**, *29*, 353.